# **Title:** Impacts on high-latitude DoD infrastructure and operations from melt events driven by large-scale low-frequency atmospheric circulations

**Proposal Number:** RC18-Z1-1658
**SERDP Project Number:** RC18-1658

**Final Report**
**Submitted 30th September 2021**
**Revised and resubmitted, 27th February 2022**

PI: Gina R. Henderson[1]
Co-PIs: Bradford S. Barrett[2], Thomas Mote[3]

[1]Oceanography Dept., U.S. Naval Academy, Annapolis MD
[2]Air Force Office of Scientific Research, Arlington, VA, United States
[3]Atmospheric Sciences Program, Geography Dept., University of Georgia, Athens, GA

# REPORT DOCUMENTATION PAGE

*Form Approved*
*OMB No. 0704-0188*



| **1. REPORT DATE** *(DD-MM-YYYY)* | **2. REPORT TYPE** | **3. DATES COVERED** *(From - To)* |
|---|---|---|
| 27/02/2022 | SERDP Final Report | |

**4. TITLE AND SUBTITLE**

Impacts on High-latitude DoD Infrastructure and Operations from Melt Events Driven by Large-scale Low-frequency Atmospheric Circulations

**5a. CONTRACT NUMBER**

**5b. GRANT NUMBER**

**5c. PROGRAM ELEMENT NUMBER**

**6. AUTHOR(S)**

Gina R. Henderson: Oceanography Dept., U.S. Naval Academy

Bradford S. Barrett: Air Force Office of Scientific Research

Thomas Mote: Atmospheric Sciences Program, Geography Dept., University of Georgia, Athens

**5d. PROJECT NUMBER**
RC18-1658

**5e. TASK NUMBER**

**5f. WORK UNIT NUMBER**

**7. PERFORMING ORGANIZATION NAME(S) AND ADDRESS(ES)**
United States Naval Academy
572 Holloway Rd.
Annapolis, MD 21402-1363

**8. PERFORMING ORGANIZATION REPORT NUMBER**
RC18-1658

**9. SPONSORING/MONITORING AGENCY NAME(S) AND ADDRESS(ES)**
Strategic Environmental Research and Development Program (SERDP)
4800 Mark Center Drive, Suite 16F16
Alexandria, VA 22350-3605

**10. SPONSOR/MONITOR'S ACRONYM(S)**
SERDP

**11. SPONSOR/MONITOR'S REPORT NUMBER(S)**
RC18-1658

**12. DISTRIBUTION/AVAILABILITY STATEMENT**

DISTRIBUTION STATEMENT A. Approved for public release: distribution unlimited.

**13. SUPPLEMENTARY NOTES**

**14. ABSTRACT**

The goal of this work was to understand and quantify the role of large-scale, lowfrequency atmospheric circulation anomalies and moisture transport on the climate system of the North Atlantic sector of the Arctic (North Atlantic Arctic, NAA). This work was motivated by recent changes in atmospheric circulation in the NAA, and their influence on sensible heat and moisture advection from the mid-latitudes into the Arctic, the surface energy budget over the Greenland Ice Sheet (GrIS) and adjacent sea ice, resulting in unprecedented melt and freshwater runoff events. Impacts of such extreme events have significant implications on DoD infrastructure and operations in the NAA, and have the potential to disrupt mission training at DoD installations across the region.

**15. SUBJECT TERMS**

Blocking, moisture transport, atmospheric teleconnections, Greenland Ice Sheet

| **16. SECURITY CLASSIFICATION OF:** | | | **17. LIMITATION OF ABSTRACT** | **18. NUMBER OF PAGES** | **19a. NAME OF RESPONSIBLE PERSON** |
|---|---|---|---|---|---|
| **a. REPORT** | **b. ABSTRACT** | **c. THIS PAGE** | | | Gina Henderson |
| UNCLASS | UNCLASS | UNCLASS | UNCLASS | 70 | **19b. TELEPHONE NUMBER** *(Include area code)* 410-476-1525 |

**Table of Contents:**

**List of Tables:**

**List of Figures:**

**Figure 9:** Frequency of extreme Greenland Blocking Index (GBI) days per year in, A) the National Center for Atmospheric Research (NCAR) model, B) the National Air and Space – Goddard Institute for Space Studies (NASA-GISS), C) the Canadian Centre for Climate Modelling and Analysis (CCCma) model, and D) the Max-Planck Institute of Meteorology (MPI), at the 90th, 95th, 97th, and 99th percentiles for June, July and August. CMIP6 models cover the time period from 1850-2015.

**Figure 10.** Frequency of above-average moisture transport for 15 days before to 15 days after an extreme blocking event in, A) the National Center for Atmospheric Research (NCAR) model, B) the National Air and Space – Goddard Institute for Space Studies (NASA-GISS), C) the Canadian Centre for Climate Modelling and Analysis (CCCma) model, and D) the Max-Planck Institute of Meteorology (MPI), at the 90th, 95th, 97th, and 99th percentiles for June, July and August. Black dashed line indicates the day of extreme blocking, and colors indicate extremity of the blocking event (from 90th to 99th percentile). CMIP6 models cover the time period from 1850-2015.

**Figure 11:** As in figure 10 for winter months (December, January and February).

**Figure 12**. (a) Annual mean bandpass filtered EKE for 1979-2018. (b) Latitude of annual mean (black line) and seasonal mean EKE (colored) at each longitude. Data were spatially smoothed with a Gaussian filter.

**Figure 13.** Time series of seasonal frequency of blocking (%) for the TM (blue), and traditional PH (purple), and modified PH (magenta) indices calculated as the total number of days per season with blocking criteria met (on the left y-axis). The monthly GBI anomalies (in meters) for the raw GBI (red) and GBI-Z (orange) are associated with the rightmost y-axis. Note: the horizontal line corresponds to where y = 0 [m] for the GBI anomaly calculations, associated with the rightmost y-axis.

**Figure 14.** Standardized seasonal blocking frequency, with respect to the 1981-2010 (1980-2009 for DJF) reference period. Year refers to the year in which December occurred.

**Figure 15.** Time series of 5-year running mean of standardized seasonal blocking frequency anomalies. Year refers to the year in which December occurred.

**Figure 16.** Total number of longitude cells per JJA season which experience blocking conditions at 54.5$^{o}$ latitude for (a) CMIP5 models and (b) CMIP6 models.

**Figure 17:** Number of days (%) with meltwater production (bar chart) and amount of meltwater production (boxplot) for blocked and unblocked conditions at Camp Century, Summit, DYE-2, and Thule.

**Figure 18:** Composite anomalies (shading) and composite means (contours: 60m interval) of 500 hPa geopotential height for all JJA blocking episode days identified separately by PH03 and GBI and composited by SOM BMU. The frequency of each node with respect to all blocking episode

days displayed in the upper right corner. Map outlines indicate subjective groupings: Omega (dark blue), CWB (medium blue), or SR (light blue).

**Figure 19:** The composite anomaly of ME for each SOM node less the composite anomaly for all blocking episode days. Contours denote MAR elevation data; contour interval of 500m from 1000–3000m.

**Figure 20:** Stripe diagram of the subjective group assignments for all cumulative JJA blocking episode days identified separately by PH03 and GBI. Stripe color denotes group assignments consistent with color-coding in Figure 19. Top axis denotes the first blocking episode day of each year. Red line shows monthly NAO index value (y-axis) for each blocking episode day. Note that the spacing of the tick marks along the top axis is proportional to the number of blocking episode days in a period—e.g., blocking frequency was greater in 2010–2015 than in 1995–2000.

**Figure 21:** Standardized counts of number of days per season with wave breaking criteria for (a) North Atlantic and (b) North Pacific. Included are all events lasting 2 or more days. A 3-year running mean is applied (bolded line). Frequencies are standardized with respect to the 1981-2010 mean. Figure from Wachowicz et al. (in prep, Clim. Dyn.).

**Figure 22:** North Atlantic %IVT relative to all RWB events lasting 3 or more days in JJA seasons of positive SST anomalies. Significance at 90% using Mann Whitney U test (red shading). Figure from Wachowicz et al. (in prep, Clim. Dyn.).

**Figure 23:** Detrended seasonal sea ice area from Walsh et al. (2019) and 3-month average detrended Niño3 (left)/ Niño4 (right) time series for the Canadian Archipelago (top) and Central Arctic (bottom). Pearson correlation (s) for JJA SSTs and 3-month average sea ice area and p-value (p) shown. Figure from Wachowicz et al. (in prep, J. Geophys. Res. Atm.).

**Figure 24:** ERA5 composites of the JJA 500 hPa height anomalies (black contours), integrated vapor transport (IVT) expressed as a % of the seasonal mean (filled), and 850 hPa seasonal mean wind (magenta) for Nino (top) and Nina (bottom) seasons. Figure from Wachowicz et al. (in prep. J. Geophys. Res. Atm.)

**Lists of Acronyms**

CMIP6: Climate Modeling Intercomparison Project 6
CWB: Cyclonic Wave Breaking
EKE: Eddy kinetic energy
GBI: Greenland Blocking Index
GrIS: Greenland Ice Sheet
IVT: Integrated Vapor Transport
NAA: North Atlantic Arctic
PH: Pelly and Hoskins Index
SOM: Self Organizing Map
TM: Tibaldi & Molteni Index

**Key words**

Blocking, moisture transport, atmospheric teleconnections, Greenland Ice Sheet

# Abstract

The goal of this work was to understand and quantify the role of large-scale, low-frequency atmospheric circulation anomalies and moisture transport on the climate system of the North Atlantic sector of the Arctic (North Atlantic Arctic, NAA). This work was motivated by recent changes in atmospheric circulation in the NAA, and their influence on sensible heat and moisture advection from the mid-latitudes into the Arctic, the surface energy budget over the Greenland Ice Sheet (GrIS) and adjacent sea ice, resulting in unprecedented melt and freshwater runoff events. Impacts of such extreme events have significant implications on DoD infrastructure and operations in the NAA, and have the potential to disrupt mission training at DoD installations across the region.

To anticipate and reduce the negative consequences of these extreme events, and to assess their impacts, this project's research objectives were to; 1) quantify the contributions from large-scale atmospheric circulation and moisture transport to ice melt events across multiple time scales, 2) understand how atmospheric blocking and Rossby wave breaking impact, and are impacted by, the transport of moisture from mid-latitudes into the NAA, and 3) investigate the role of this moisture advection in altering radiative and turbulent fluxes, winds, precipitation, surface melting, and snow accumulation in the NAA.

To accomplish the overarching research goal and the three objectives stated above, our research tasks included; creation of a moisture transport and blocking climatology in the NAA region using a variety of blocking metrics, assessment of the impact of Rossby Wave Breaking on moisture transport into the NAA region, and finally quantification of such relationships and mechanisms in future climate scenarios via the use of climate model ensemble output.

Results of this project have shown that it is critical to understand patterns of atmospheric circulation in the high latitudes, including when those patterns are disrupted, which happens during atmospheric blocking events. We found that blocking has the potential to significantly impact the Greenland ice sheet via rapid melting and runoff, depending on the location where the blocking pattern sets up. We also found trends toward more periods of extreme blocking in the most recent 20 years, and continue to analyze whether that trend appears in sophisticated climate model predictions of the coming decades. In terms of types of blocking episodes, summer ridge patterns produced more melt over the southern Greenland ice sheet, with Omega blocks producing more melt across the northern ice sheet, and cyclonic wave breaking patterns producing more melt in northeast Greenland. While occurrences of the Omega blocking pattern have increased more than other blocking types, the number of days in the North Atlantic exhibiting cyclonic wave breaking characteristics in June, July and August have significantly increased, which corresponds to observed increased Greenland blocking conditions and increased moisture transport.

More work is needed on blocking's impacts on specific sensitive DoD infrastructure and operations in Greenland, including and specifically at Thule Air Base, which is now home to critical operations of USSF Delta 2 (space situational awareness) and Delta 4 (spaceborne missile detection) groups.

## Executive Summary:

The goal of this work was to understand and quantify the role of large-scale, low-frequency atmospheric circulation anomalies and moisture transport on the climate system of the North Atlantic sector of the Arctic (North Atlantic Arctic, NAA). Recent changes in low-frequency atmospheric circulation in the NAA have increased sensible heat and moisture advection from the mid-latitudes into the Arctic. This, in turn, has altered the surface energy budget over the Greenland Ice Sheet (GrIS) and adjacent sea ice and contributed to unprecedented melt and freshwater runoff events. For example, the extreme 2012 melt across Greenland, which was followed by other intense melt events in subsequent years along with record or near-record warmth and lack of sea ice in the Arctic Ocean, provide an exceptional opportunity for timely investigation on the multiple ways in which large-scale atmospheric circulation drives land- and sea-ice changes across the NAA. These extreme events have significant and yet unexplored impacts on DoD infrastructure and operations in the NAA: freshwater runoff alters acoustic profiles of subsurface waters adjacent to DoD installations in Greenland; warmer air and ocean temperatures open surface transit lanes in newly ice-free areas; surface melt leads to uncertain aircraft operations on the GrIS; increased melt challenges waste management at legacy infrastructure on the GrIS; and unusual wind, visibility, precipitation, and ice all disrupt mission training at DoD installations across the region.

To anticipate and reduce the negative consequences of these extreme events, the objectives of this research were to:

1. Quantify the contributions from large-scale atmospheric circulation and moisture transport to ice melt events across multiple time scales;
2. Understand how atmospheric blocking and Rossby wave breaking impact, and are impacted by, the transport of moisture from mid-latitudes into the NAA; and
3. Investigate the role of this moisture advection in altering radiative and turbulent fluxes, winds, precipitation, surface melting, and snow accumulation in the NAA.

Both theoretical and modeling studies predict increasing poleward moisture transport in a warming climate (Lavers et al. 2015). This is supported by observations of Arctic moistening trends (Mattingly et al. 2020). Heat can be transported into the Arctic by winds, for example, tropical warming caused by El Niño or anthropogenic warming can cause shifts in atmospheric weather patterns, which may lead to changes in surface temperatures the Arctic. Clear, warm conditions may precondition the surface prior to the onset of an atmospheric river (moisture transport), which enhances melt energy.

Atmospheric blocking, and specifically Greenland Blocking, is characterized by unusual waviness in the jet stream centered over Greenland (Fig. 1, left). Implications of Greenland blocking include warmer temperatures and more frequent melt events over the GrIS, in addition to colder temperatures and snow over the U.S. and Europe. Impacts of Greenland Blocking to Department of Defense (DoD) operations (Fig.1, right) in the high-latitudes include changes in sea ice concentration, snow and ice melt, freshwater input changes to the expected acoustic profile and unusual cloud cover and precipitation throughout the region. In addition, most poleward moisture transport occurs in atmospheric rivers (ARs), which are often associated with atmospheric blocking (Mattingly et al. 2018). This was particularly evident during the extreme melt event in July 2012, when virtually the entire GrIS experienced surface melt for the first time in over a century. Strong ARs increase GrIS summer melt, especially in the ablation zone.

Increased moisture transport by ARs to West Greenland played a key role in GrIS mass loss, whereas sea ice loss in the Arctic is also associated with AR activity.

Motivated by the links between Greenland blocking, moisture transport and implications for extreme surface melt, this project sought to **assess the impact of large-scale atmospheric circulation & moisture transport on high-latitude DoD operations and installations in the North Atlantic Sector of the Arctic**. To accomplish this overarching research goal, and the three objectives stated above, our research tasks included:

**Research Task #1 -** ***Create a moisture transport and blocking climatology (1980-present) in the NAA region.*** To accomplish this task, a variety of blocking metrics were utilized to identify blocking events. The use of multiple metrics was necessary as it has been established by the scientific community that identification of blocking events is sensitive to a variety of factors, and can vary depending on which metric is used. For this reason, our team explored multiple metrics, such as that outlined in Tibaldi and Molteni (1990), in Pelly and Hoskins (2003), and in Hanna et al. (2013). Metrics of moisture transport included primarily vertically integrated horizontal water vapor transport. To ensure a robust result, an ensemble approach using multiple high-quality atmospheric reanalysis products, including the ECMWF Reanalysis (ERA) -Interim and version 5 (ERA5) data were used.

**Research Task #2 -** ***Assess the impact of Rossby Wave Breaking on moisture transport into the NAA region.*** We adopted an approach similar to that of Liu and Barnes (2015) to explore the impact of Rossby Wave Breaking on moisture transport into our region of interest, using contours of potential temperature and moisture transport fields to identify specific patterns of extreme moisture transport. This was conducted using the same reanalysis products as in task #1. In addition, several large-scale, low-frequency teleconnection patterns, such as El Nino Southern Oscillation was used to assess how moisture transport is related to changes in atmospheric circulation in the NAA region on both interannual to intra-seasonal timescales.

**Research Task #3 -** ***Quantify the relationships identified in tasks #1 and #2 in future climate scenarios.*** An ensemble approach was used to understand how well patterns of large-scale atmospheric variability are represented in the Climate Model Intercomparison Project (CMIP)-6 models. The focus of this task was to assess how blocking was represented in a selection of historical runs within the CMIP6 suite, using composites of atmospheric moisture and energy budget components to investigate the magnitude of the impact on the Greenland ice sheet and sea ice in the NAA. The composites included the above-mentioned impact-driven surface meteorological (e.g., wind, precipitation) and cryospheric (e.g. surface melt, sea ice concentration) fields.

Objective 1 was largely achieved by the development of a Greenland blocking and moisture climatology using both atmospheric reanalysis products and climate model output. Key findings relating to these objectives include the following:

- Extreme atmospheric flow blocking over Greenland has increased in the period 2000-2019 compared to 1980-1999. The increase has been seen in both winter (December-February) and summer (June-August). Moreover, blocking was found to exhibit some interannual

variability, in agreement with McLeod and Mote (2015), whereby years with frequent extreme blocking and years with scarce extreme blocking tending to cluster together (Fig. 4).

- Atmospheric moisture transport is associated with extreme flow blocking in and around Greenland in both seasons. Above-normal moisture transport (quantified by integrated vapor transport, IVT) over Greenland seems to lead, rather than lag, extreme blocking, by an average of three days (Fig. 6). These findings are unique to this work and lead to questions about the role of moisture transport in developing or sustaining blocks over Greenland, related to questions posed by McLeod and Mote (2015b) on the role of precursor cyclones.
- Greenland blocking calculated from the Greenland Blocking Index (GBI) shows an increase in blocking for DJF and MAM with significant increases in JJA; once detrended, the GBI, Tibaldi and Molteni (TM) and Pelly and Hoskins (PH) indices suggest an insignificant decrease in blocking during SON and DJF and increase in blocking during MAM and JJA. However, the use of one particular metric over another may limit the assessment of individual case studies (Fig. 14).
- The use of a constant latitude in identifying instantaneous Arctic blocking in the CMIP5 and CMIP6 models has limitations regarding the frequency of blocking more so than the preferred regions of blocking. Despite this, CMIP6 models appear to better represent blocking conditions over the 1979-2004 period when compared to CMIP5. Furthermore, the inclusion of eddy kinetic energy (EKE) in defining blocking may improve current Arctic blocking climatologies in climate models (Fig. 16).

In terms of objective 2, Rossby wave breaking and its relationship to Greenland blocking and moisture transport into the NAA, and objective 3, the role of this moisture advection in altering the surface energy balance and subsequent influence in melt events, some key findings included:

- Relative to all blocking episodes, summer ridge patterns produce more melt over the southern ice sheet, Omega blocks produce more melt across the northern ice sheet, and cyclonic wave breaking patterns produce more melt in northeast Greenland (Fig. 18 and 19).
- Distinct mechanisms of melt production for each blocking type include: lower-amplitude, summer ridge patterns direct onshore moisture transport into southwest Greenland, generating above-normal longwave downward radiation and increased sensible heat flux that aligns with relatively more melt over the southern ice sheet than other blocking types; cyclonic wave breaking patterns produce an apparent foehn effect where cross-barrier flow generates above-normal incoming shortwave radiation and enhanced sensible heat flux that accompanies relatively more melt over northeast Greenland; and high-amplitude, Omega blocking directs onshore flow over the northwestern and northern coastlines, generating above-normal longwave downward radiation that aligns with relatively greater melt across the northern GrIS. Moreover, the location and frequency of Greenland blocking may impact heat and moisture transport near Thule. This poses significant threat on Thule's infrastructure, as increased liquid precipitation and warmer temperatures will act to accelerate permafrost melt.
- Omega blocking patterns have increased more than other blocking types. Given the failure of global climate models to resolve the overall increase in Greenland blocking (Hanna et al. 2018; Slater et al. 2020), if the increase in Omega blocking were to continue, it would likely result in the underestimation of future GrIS melt. This is particularly true for the northern ice sheet where Omega blocks produce more melt than other blocking types, which has important implications for surface mass loss over Camp Century and runoff near Thule.

- The number of days in the North Atlantic exhibiting cyclonic wave breaking (CWB) characteristics in JJA have significantly increased (Fig. 21), which corresponds to observed increased Greenland blocking conditions and increased moisture transport. This is important considering our findings suggest higher IVT under CWB conditions, especially in JJA. Higher IVT values are present during Central Pacific El Nino when compared to EP El Nino, further demonstrating tropical influences of NAA hydroclimatology.
- Summer sea ice in the Canadian Archipelago and Central Arctic regions appears most sensitive to the Central Pacific El Niño, resulting in less sea ice loss. While this may be due to springtime sea ice-ENSO connections, the increase in moisture transport during Central Pacific ENSO events within the region and its impact on the sea ice warrants further investigation (Fig. 23). The connection between these mechanisms is not prevalent in CESM LENS, and should be investigated in CESM2 and other CMIP6 models.

In summary, the results of this project have shown that it is critical to understand patterns of atmospheric circulation in the high latitudes, including when those patterns are disrupted, which happens during blocking. We found that blocking has the potential to significantly impact the Greenland ice sheet. It can provoke rapid melting and runoff, depending on the location where the blocking pattern sets up. We also found trends toward more periods of extreme blocking in the most recent 20 years, and will continue analyzing whether that trend appears in sophisticated climate model predictions of the coming decades.

More work is needed on blocking's impacts on specific sensitive DoD infrastructure and operations in Greenland, including and specifically at Thule Air Base, which is now home to critical operations of USSF Delta 2 (space situational awareness) and Delta 4 (spaceborne missile detection) groups. This work will be explored in an extension of this project, in which we seek to assess the climate security of northwest Greenland by investigating and understanding trends in past and expected future climate of the region. We will leverage the findings of this project, transitioning basic research to support critical DoD base infrastructure integral to current and future Space Force endeavors. Specifically, we will focus on Thule Air Base and the surface conditions that adversely affect base operations and the surrounding region, in addition to improving spatial representation in global Earth system models.

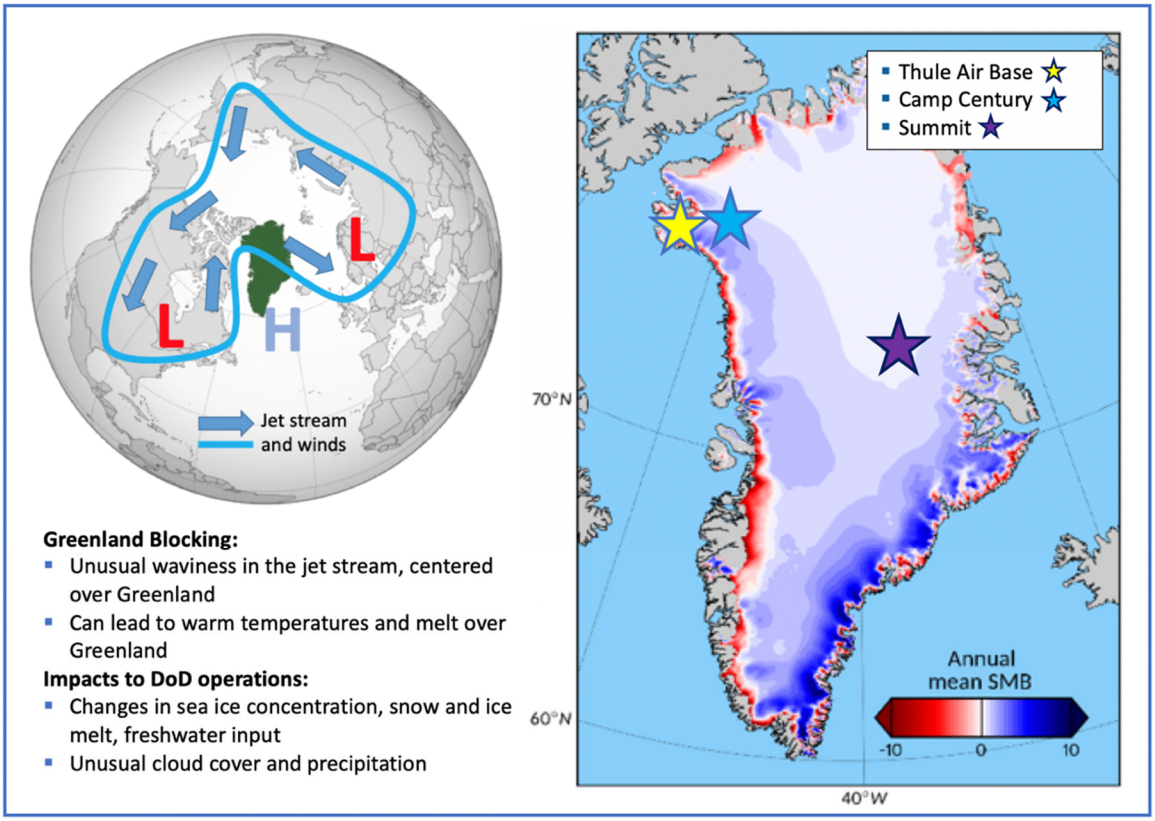


**Figure 1:** Schematic highlighting both the spatial extent and physical implications of Greenland Blocking (left), and the implications for high-latitude Department of Defense (DoD) operations (right).

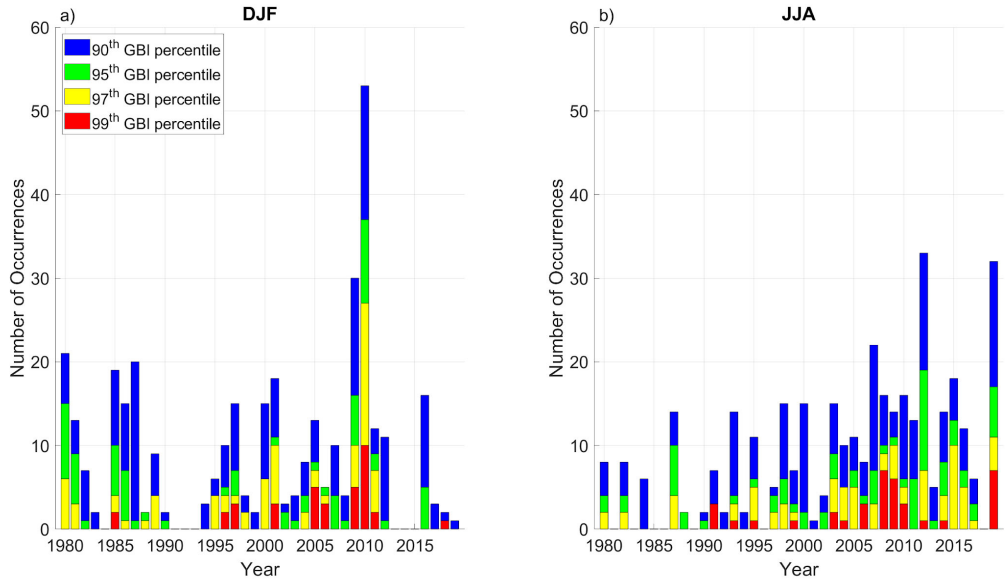


**Figure 4:** Frequency of extreme Greenland Blocking Index (GBI) days per year in the ERA-Interim reanalysis product (1980-2019) in (a) DJF and (b) JJA, at the 90th, 95th, 97th, and 99th percentiles for each season (Barrett et al. 2020).

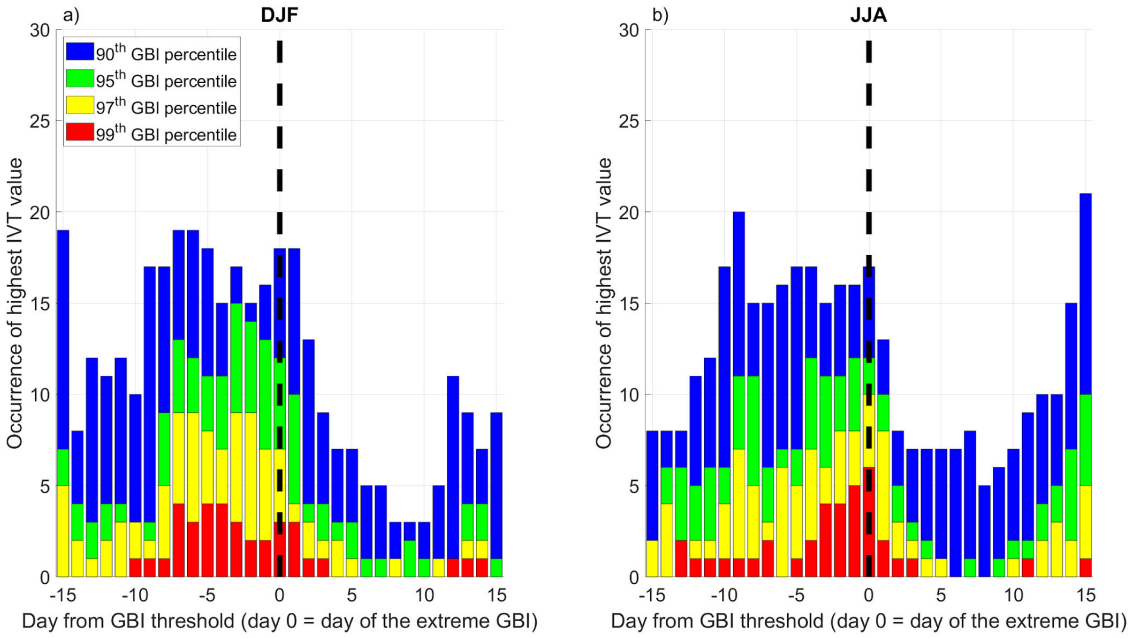


**Figure 6:** Frequency of above-average moisture transport for 15 days before to 15 days after an extreme blocking event in (a) DJF and (b) JJA in the ERA-Interim reanalysis product. Black dashed line indicates the day of extreme blocking, and colors indicate extremity of the blocking event (from 90th to 99th percentile). Figure from Barrett et al. 2020.

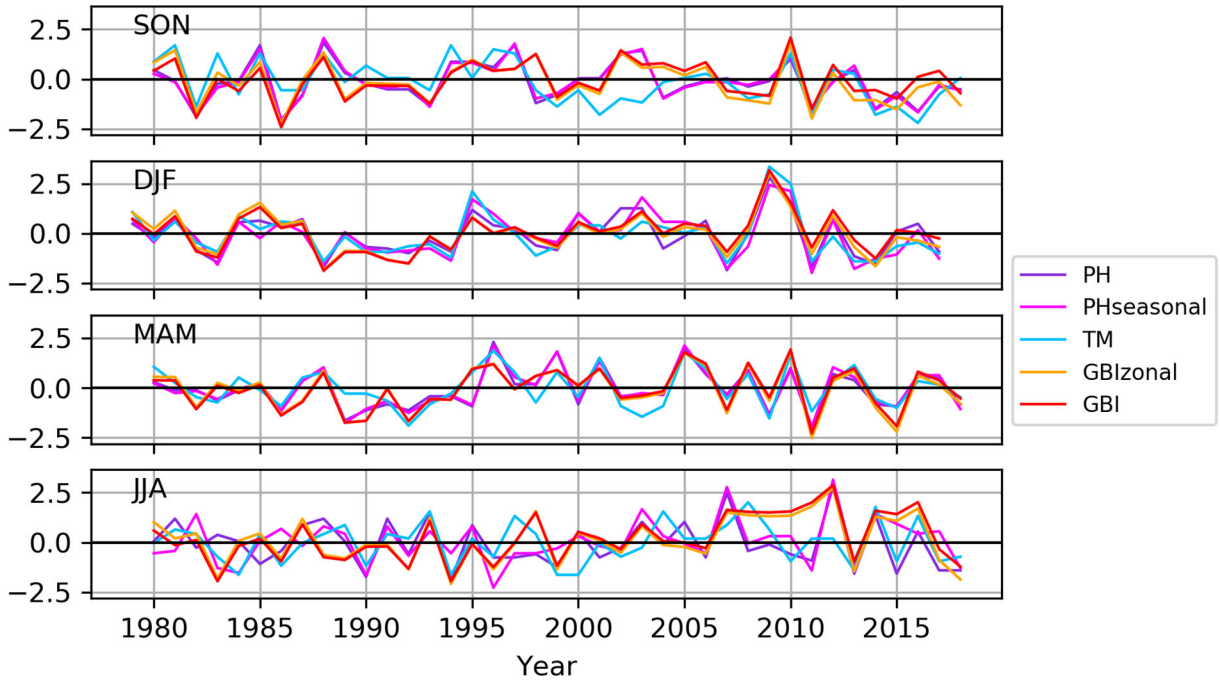


**Figure 14.** Standardized seasonal blocking frequency, with respect to the 1981-2010 (1980-2009 for DJF) reference period. Year refers to the year in which December occurred. Figure from Wachowicz et al. 2020.

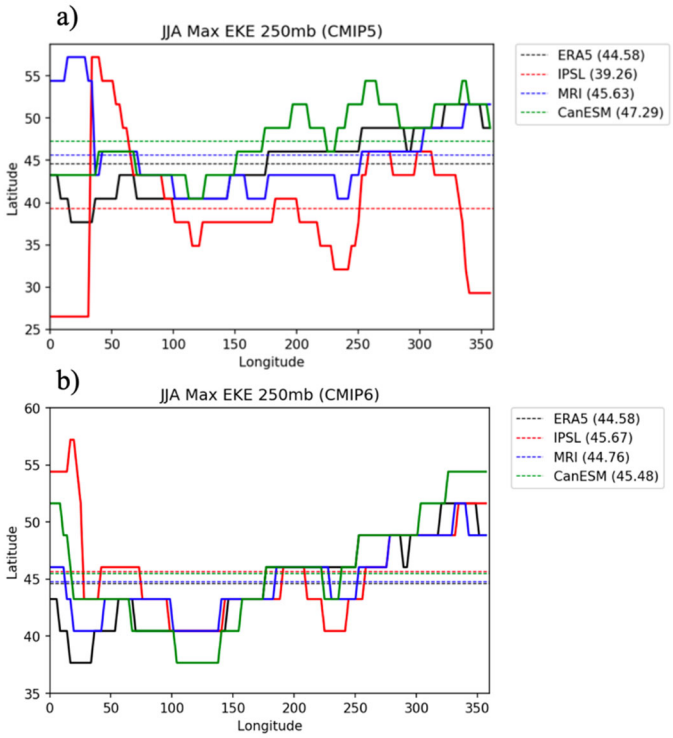


**Figure 16.** Total number of longitude cells per JJA season which experience blocking conditions at 54.5$^{o}$ latitude for (a) CMIP5 models and (b) CMIP6 models.

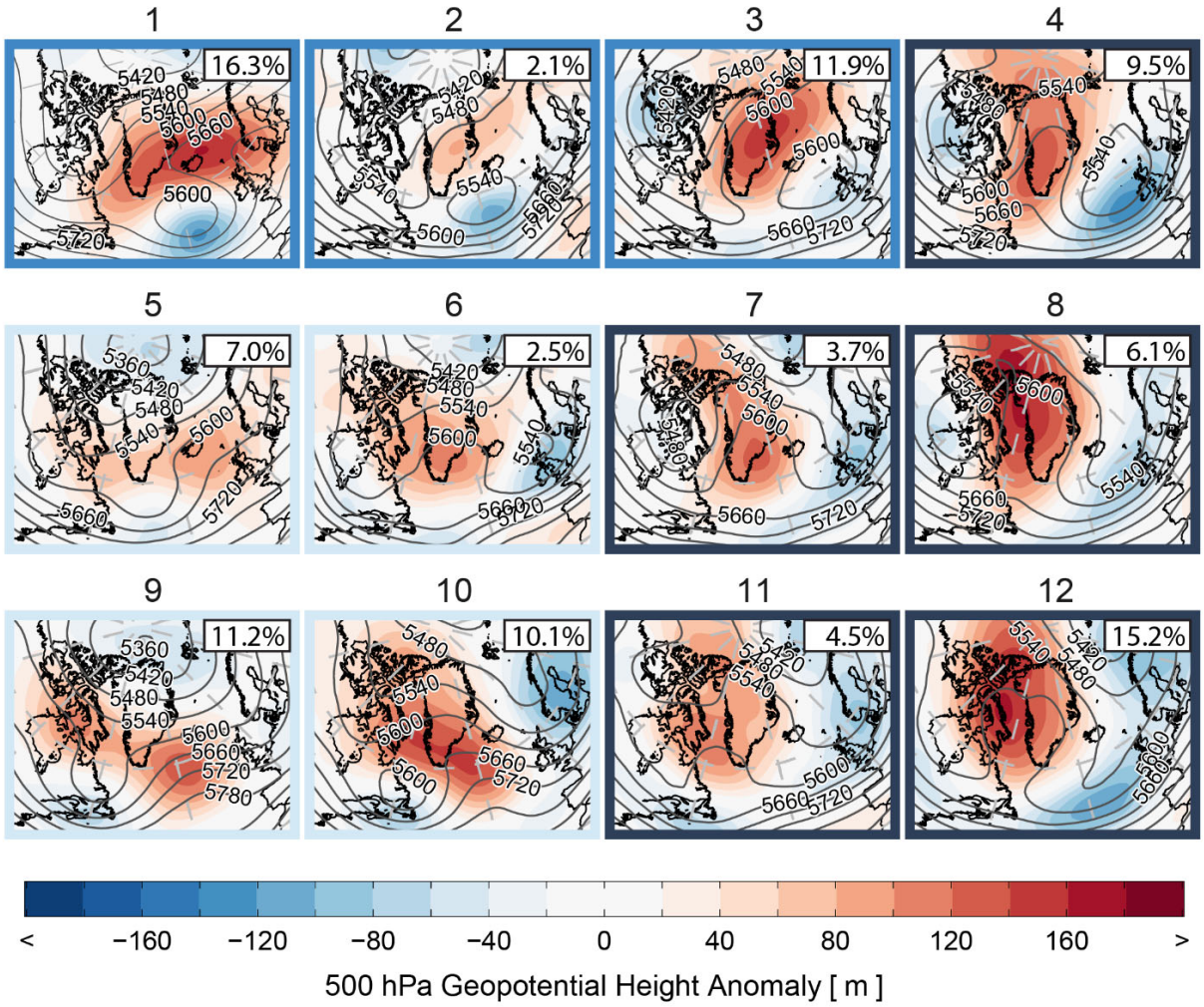


**Figure 18:** Composite anomalies (shading) and composite means (contours: 60m interval) of 500 hPa geopotential height for all JJA blocking episode days identified separately by PH03 and GBI and composited by SOM BMU. The frequency of each node with respect to all blocking episode days displayed in the upper right corner. Map outlines indicate subjective groupings: Omega (dark blue), CWB (medium blue), or SR (light blue). Figure from Preece et al. 2022.

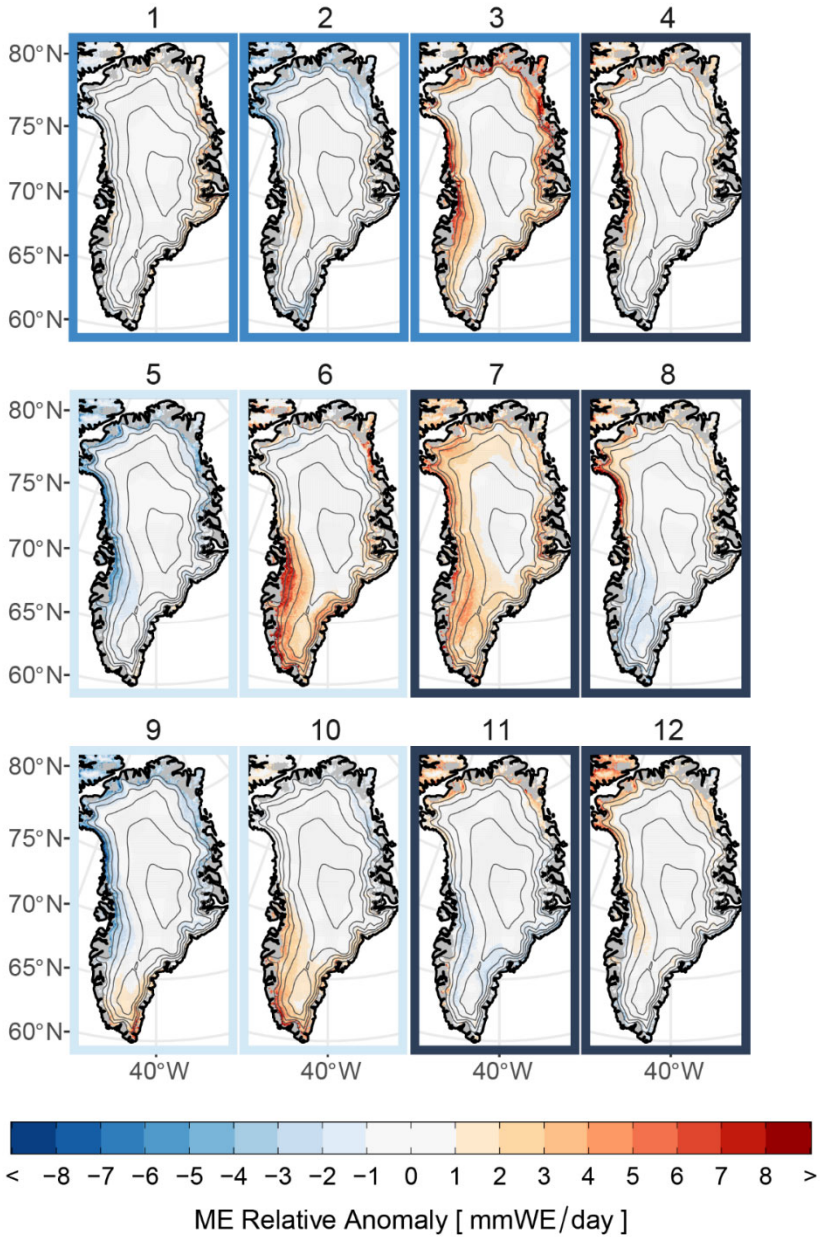


**Figure 19:** The composite anomaly of ME for each SOM node less the composite anomaly for all blocking episode days. Contours denote MAR elevation data; contour interval of 500m from 1000–3000m. Figure from Preece et al. 2022.

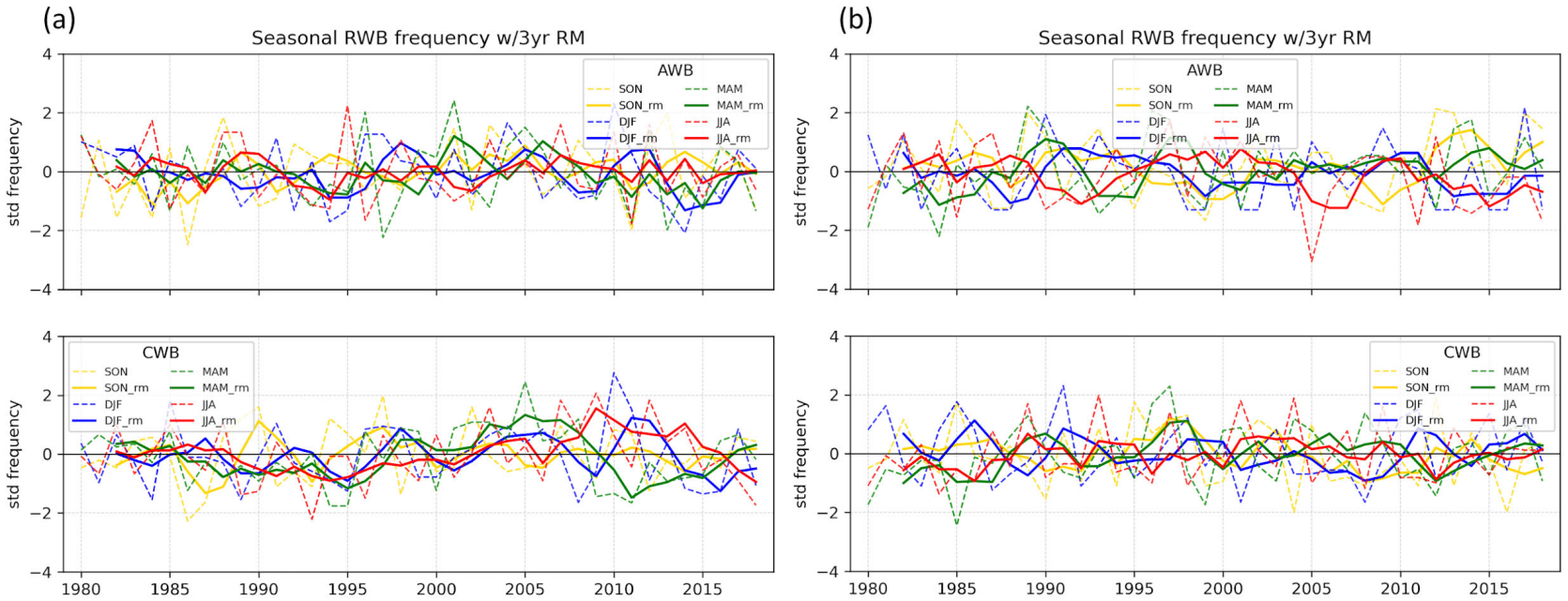


**Figure 21:** Standardized counts of number of days per season with wave breaking criteria for (a) North Atlantic and (b) North Pacific. Included are all events lasting 2 or more days. A 3-year running mean is applied (bolded line). Frequencies are standardized with respect to the 1981-2010 mean. Figure from Wachowicz et al. (in prep, Clim. Dyn.).

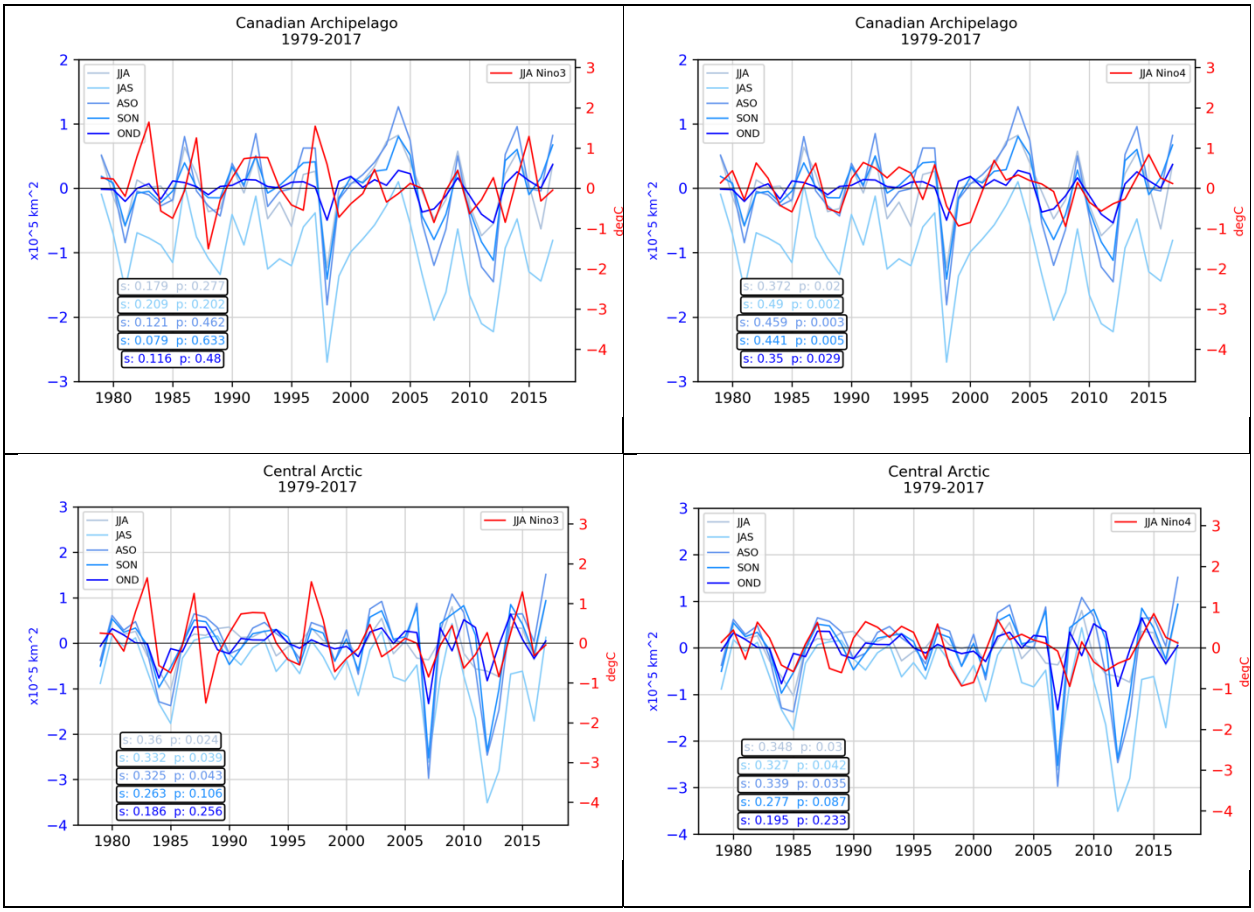


**Figure 23:** Detrended seasonal sea ice area from Walsh et al. (2019) and 3-month average detrended Niño3 (left)/ Niño4 (right) time series for the Canadian Archipelago (top) and Central Arctic (bottom). Pearson correlation (s) for JJA SSTs and 3-month average sea ice area and p-value (p) shown. Figure from Wachowicz et al. (in prep, J. Geophys. Res. Atm.).

# Objective:

The goal of this work was to understand and quantify the role of large-scale, low-frequency atmospheric circulation anomalies and moisture transport on the climate system of the North Atlantic sector of the Arctic (North Atlantic Arctic, NAA). Recent changes in atmospheric circulation in the NAA have increased sensible heat and moisture advection from the mid-latitudes into the Arctic. This, in turn, has altered the surface energy budget over the Greenland Ice Sheet (GrIS) and adjacent sea ice and contributed to unprecedented melt and freshwater runoff events. For example, the extreme 2012 melt across Greenland, which was followed by other intense melt events in subsequent years along with record or near-record warmth and lack of sea ice in the Arctic Ocean, provide an exceptional opportunity for timely investigation on the multiple ways in which large-scale atmospheric circulation drives land- and sea-ice changes across the NAA. These extreme events have significant and yet unexplored impacts on DoD infrastructure and operations in the NAA: freshwater runoff alters acoustic profiles of subsurface waters adjacent to DoD installations in Greenland; warmer air and ocean temperatures open surface transit lanes in newly ice-free areas; surface melt leads to uncertain aircraft operations on the GrIS; increased melt challenges waste management at legacy infrastructure on the GrIS; and unusual wind, visibility, precipitation, and ice all disrupt mission training at DoD installations across the region.

To anticipate and reduce the negative consequences of these extreme events, the objectives of this research were to:

1. Quantify the contributions from large-scale atmospheric circulation and moisture transport to ice melt events across multiple time scales;
2. Understand how atmospheric blocking and Rossby wave breaking impact, and are impacted by, the transport of moisture from mid-latitudes into the NAA; and
3. Investigate the role of this moisture advection in altering radiative and turbulent fluxes, winds, precipitation, surface melting, and snow accumulation in the NAA.

Both theoretical and modeling studies predict increasing poleward moisture transport in a warming climate (Lavers et al. 2015). This is supported by observations of Arctic moistening trends (Mattingly et al. 2020). Heat can be transported into the Arctic by winds, for example, tropical warming caused by El Niño or anthropogenic warming can cause shifts in atmospheric weather patterns, which may lead to changes in surface temperatures the Arctic. Clear, warm conditions may precondition the surface prior to the onset of an atmospheric river (moisture transport), which enhances melt energy.

Atmospheric blocking, and specifically Greenland Blocking, is characterized by unusual waviness in the jet stream centered over Greenland (Fig. 1, left). Implications of Greenland blocking include warmer temperatures and more frequent melt events over the GrIS, in addition to colder temperatures and snow over the U.S. and Europe. Impacts of Greenland Blocking to Department of Defense (DoD) operations (Fig.1, right) in the high-latitudes include changes in sea ice concentration, snow and ice melt, freshwater input changes to the expected acoustic profile and unusual cloud cover and precipitation throughout the region. In addition, most poleward moisture transport occurs in atmospheric rivers (ARs), which are often associated with atmospheric blocking (Mattingly et al. 2018). This was particularly evident during the extreme melt event in July 2012, when virtually the entire GrIS experienced surface melt for the first time in over a century. Strong ARs increase GrIS summer melt, especially in the ablation zone.

Increased moisture transport by ARs to West Greenland played a key role in GrIS mass loss, whereas sea ice loss in the Arctic is also associated with AR activity.

Motivated by the links between Greenland blocking, moisture transport and implications for extreme surface melt, this project sought to **assess the impact of large-scale atmospheric circulation & moisture transport on high-latitude DoD operations and installations in the North Atlantic Sector of the Arctic**. To accomplish this overarching research goal, and the three objectives stated above, our research tasks included:

**Research Task #1 -** ***Create a moisture transport and blocking climatology (1980-present) in the NAA region.*** To accomplish this task, a variety of blocking metrics were utilized to identify blocking events. The use of multiple metrics was necessary as it has been established by the scientific community that identification of blocking events is sensitive to a variety of factors, and can vary depending on which metric is used. For this reason, our team explored multiple metrics, such as that outlined in Tibaldi and Molteni (1990), in Pelly and Hoskins (2003), and in Hanna et al. (2013). Metrics of moisture transport included primarily vertically integrated horizontal water vapor transport. To ensure a robust result, an ensemble approach using multiple high-quality atmospheric reanalysis products, including the ECMWF Reanalysis (ERA) -Interim and version 5 (ERA5) data were used.

**Research Task #2 -** ***Assess the impact of Rossby Wave Breaking on moisture transport into the NAA region.*** We adopted an approach similar to that of Liu and Barnes (2015) to explore the impact of Rossby Wave Breaking on moisture transport into our region of interest, using contours of potential temperature and moisture transport fields to identify specific patterns of extreme moisture transport. This was conducted using the same reanalysis products as in task #1. In addition, several large-scale, low-frequency teleconnection patterns, such as El Nino Southern Oscillation was used to assess how moisture transport is related to changes in atmospheric circulation in the NAA region on both interannual to intra-seasonal timescales.

**Research Task #3 -** ***Quantify the relationships identified in tasks #1 and #2 in future climate scenarios.*** An ensemble approach was used to understand how well patterns of large-scale atmospheric variability are represented in the Climate Model Intercomparison Project (CMIP)-6 models. The focus of this task was to assess how blocking was represented in a selection of historical runs within the CMIP6 suite, using composites of atmospheric moisture and energy budget components to investigate the magnitude of the impact on the Greenland ice sheet and sea ice in the NAA. The composites included the above-mentioned impact-driven surface meteorological (e.g., wind, precipitation) and cryospheric (e.g. surface melt, sea ice concentration) fields.

Specific details of the methods used in each of these tasks are described in the Materials and Methods section below.

## Background:

Atmospheric flow blocking can be defined by the appearance of an anomalous center of high pressure or mid-tropospheric ridge, many times off the western margin of continents, that deflects traveling cyclones from their usual storm tracks (Rex, 1950a,b; Namias, 1982; Rasmussen and Wallace, 1983; Legras and Ghil, 1985). This anticyclone is often associated with a breakdown of the high kinetic energy state of the atmosphere into a low kinetic energy state, possibly even reversing mid-latitude westerly flow to easterly (Tibaldi and Molteni, 1990; Scherrer et al., 2006; Tyrlis and Hoskins, 2008). Atmospheric blocking can cause a strong equatorward deflection of polar air on the eastern flank of the anticyclone, leading to severe cold episodes in winter (Dole and Gordon, 1983; Hoskins and Sardeshmukh, 1987) and severe droughts and heat waves in summer (Black et al., 2004; Dole et al., 2011). Over Greenland, flow blocking results in a large-scale reversal of the meridional geopotential height gradient, a potential increase in surface temperature (Pelly and Hoskins, 2003), and possible changes in ice mass balance (McLeod and Mote, 2016). The occurrence of flow blocking is thus of critical interest to both weather and climate, and in our case circulation in the NAA.

Many metrics have been created to identify and quantify atmospheric flow blocking. Some involve hierarchical methods (spatial clustering; Cheng and Wallace, 1993) and non-hierarchical (partitioning) methods (Michelangeli et al., 1995), while others use mixture model (Smyth et al., 1999) and nonlinear equilibrium methods (Vautard, 1990). Still other techniques involve measures of the strength of the westerly flow (Tibaldi and Molteni, 1990; Pelly and Hoskins, 2003), both of which were used extensively in this project. In addition, a Greenland Blocking Index (GBI) defined by Fang (2004) to examine atmospheric flow blocking over and around Greenland, has found many uses (Hanna et al., 2013; 2014; 2015), perhaps owing to its ability to clearly and simply depict blocking—and changes in blocking— across the Greenland region. This GBI index was used extensively in this study.

Moisture and moisture transport in the Arctic have received renewed attention recently, partly because of strong warming in surface temperatures in this region, significantly above worldwide trends (Polyakov et al., 2002; Serreze et al., 2009; Screen and Simmonds, 2010; Hartmann et al., 2013). The northern North Atlantic stands out as a main gateway for moisture transport to the Arctic, and that channel is linked strongly to transient eddies in the mean circulation, particularly for southwest Greenland (Dufour et al., 2016). Overall, the Arctic atmosphere north of 70°N has been steadily moistening (Held and Soden, 2006; Gimeno et al., 2014; Lavers et al., 2015; Rinke et al., 2019). Over Greenland, "moist" days (defined as days with anomalously high water vapor transport to Greenland) have increased in frequency between 1979 and 2015 (Mattingly et al., 2016). Summer moisture transport over Greenland has tended to receive the most attention in the literature (Yang and Magnusdottir, 2017; Mattingly et al., 2018), due to its link to surface ice mass balance, but transient eddy fluxes over the Greenland Sea (east of Greenland) are comparable for both winter and summer (Dufour et al., 2016).

Along with the rapid warming across much of the Arctic region via a variety of feedbacks within the Earth system through a process known as Arctic amplification (Serreze and Francis, 2006; Dai et al., 2019), which is a motivating factor for this work, recent work has found that this warming has led to a weakening of the zonal winds and a waiver, higher-amplitude jet stream. This in turn has resulted in the slower propagation of Rossby waves (Francis and Vavrus, 2012, 2015; Luo et al., 2018). Rossby wave breaking (RWB), may act to decrease the speed and vary the position of the eddy-driven jet (Barnes et al., 2010; Ronalds et al., 2018; Woollings et al.,

2018), leading to more persistent weather conditions related to blocking. Such mechanisms can lead to more extreme and frequent atmospheric blocks, therefore the mechanism of RWB was a key process explored in this work to connect the dynamics of the NAA to blocking occurrences. In addition, RWB and blocking has been linked to moisture transport in the Arctic (Woods et al., 2013), including more distant moisture sources during periods of high Greenland blocking (Nusbaumer et al., 2019), and southwest Greenland has emerged as perhaps a favored channel and impact zone for that transport (Liu and Barnes, 2015).

To better understand and quantify impacts of low-frequency atmospheric circulations on GrIS melt, surface energy balance, mass balance, and sea ice variability, a long-term (1980-present), systematic investigation of moisture transport and blocking in the NAA region was conducted over the course of this project using a variety of metrics that will be discussed in more detail in the following section. The impact of RWB on moisture transport into the NAA region was be explored using an approach similar to that of Liu and Barnes (2015), which will also be discussed in greater detail below.

## Materials and Methods:

In this section, the primary data products, metrics and statistical techniques used to accomplish research tasks 1-3 will be summarized. The current study did not involve any field work, and all data products utilized were publicly available.

**Research Task #1 data and techniques:** To create both the moisture transport and blocking climatologies, two publicly available data sets were utilized. First, Greenland blocking was quantified using the daily GBI (Hanna et al., 2013) over the 40-year period January 1980 to December 2019. The GBI is the mean 500-hPa geopotential height over the Greenland region, from 20° to 80°W and 60° to 80°N (Fig. 2), and the daily index is available from https://www.esrl. noaa.gov/psd/data/timeseries/daily/GBI/. For our project, a "block" refers to an instantaneous block, including transient high-pressure systems and persistent blocking events, and does not distinguish between the two. Extreme blocking was calculated for summer (June to August; JJA) and winter (December to February; DJF) by identifying the daily GBI values that correspond to four thresholds of extremity: the 90th, 95th, 97th, and 99th percentiles. Physically, an extreme positive GBI indicates highly anomalous instantaneous ridging over Greenland (McCloud and Mote, 2015), and in this case, the mean height field during the 95th percentile featured instantaneous ridging centered over southeast Greenland in winter (DJF) and south-central Greenland in summer (JJA) (Fig. 2). To quantify moisture transport over Greenland, integrated vapor transport (IVT) was used, which was calculated from the ERA-interim reanalysis (Dee et al., 2011), following the methodology of Rutz et al. (2014) and Mattingly et al. (2016):

$$IVT = \frac{1}{g}\int_{1000\ hPa}^{200hPa} q\,V dp$$

where q and V are the specific humidity (in $kg \cdot kg^{-1}$) and wind vector (in $m \cdot s^{-1}$) at pressure level p, dp is the difference between consecutive pressure levels (50-hPa intervals between 1,000 and

500 hPa and 100-hPa intervals between 500 and 200 hPa), and g is the gravitational acceleration (9.80655 $m \cdot s^2$). Daily IVT values were calculated at 1200 UTC each day from January 1980 to August 2019 at each grid point in the ERA-interim reanalysis. To examine moisture transport around Greenland specifically, IVT was spatially averaged over the region from 15° to 85°W and 55° to 80°N (Fig. 3). Extreme values of IVT at the 90th, 95th, 97th, and 99th percentiles for both DJF and JJA.

In addition to the use of the GBI blocking metric, additional blocking indices were considered. This work was conducted using daily ECMWF Reanalysis version 5 (ERA5) data at a 1° spatial resolution for the period of January 1979 through December 2018 (Hersbach et al., 2020). Variables used include: 500 hPa geopotential height (m), and temperature (K), potential vorticity (PV) ($Km^2 \cdot kg^{-1} \cdot s^{-1}$), u- and v-winds ($m \cdot s^{-1}$) at all pressure levels. Potential temperature was calculated at all pressure levels then linearly interpolated to a constant PV surface. The Tibaldi and Molteni blocking index (TM) identifies in the 500 hPa field reversals of the geopotential height (Z) gradients to the north and south of a given latitude. The southward gradient (GHGS) and northward gradient (GHGN) are calculated as:

$$GHGS = \frac{Z(\phi_o) - Z(\phi_s)}{\phi_o - \phi_s}$$

$$GHGN = \frac{Z(\phi_n) - Z(\phi_o)}{\phi_n - \phi_o}$$

where $\varphi_n = 80°N$ $\varphi_o = 60°N$, $\varphi_s = 40°N$. As described in Tibaldi and Molteni (1990), for blocking conditions to be present at a given longitude, GHGS >0 and GHGN < −10 m/deg latitude for at least one of the calculations. We considered a day with blocking conditions for Greenland if the longitudinal extent of the block spans at least 12° longitude within the GBI domain, which is the minimal spatial extent required to be considered a block.

Finally, unlike the GBI and TM indices which exclusively use geopotential height data, the Pelly and Hoskins index (PH) utilized potential temperature (Θ) on a constant potential vorticity (PV) surface of 2 potential vorticity units (2PVU) to identify reversals of the meridional potential temperature gradient. For the PH index, blocking for a given longitude is calculated as:

$$B = \frac{2}{\Delta\phi}\int_{\phi_o}^{\phi_o + \Delta\phi/2} \theta d\phi - \frac{2}{\Delta\phi}\int_{\phi_o - \Delta\phi/2}^{\phi_o} \theta d\phi$$

Where $\varphi_o$ is the central blocking latitude and $\Delta\varphi = 30°$ is the latitudinal range over which the gradient is calculated. Under this definition, B > 0 indicates a reversal of the gradient, thus corresponding to blocking. This method is argued to provide a more dynamic approach to identifying blocking events, as instantaneous blocking at a given longitude varies by latitude (Pelly and Hoskins 2003).

Following Pelly and Hoskins (2003), the latitude by which the meridional temperature gradient, the central blocking latitude (CBL, $\phi_o$), is identified as the latitude of maximum annual eddy kinetic energy (EKE) at 300 hPa (Fig. 12). To account for synoptic scale eddies, we apply a 2.5 to 10-day bandpass filter on the u- and v-winds prior to calculating annual EKE (Blackmon and White, 1982) (Fig. 8a). We calculate EKE as follows:

$$EKE = \frac{1}{2}(u' + v')^2$$

where u' and v' are the bandpass filtered u- and v- winds. From here, we extract the maximum B value for $\phi_o = \phi_c$ +/- $\Delta$, where $\Delta = 4°$, similar to the TM index, for each longitude.

**Research Task #2 techniques:** To explore the impact of Rossby Wave Breaking (RWB) on moisture transport into our region of interest, we adopted an approach similar to that of Liu and Barnes (2015), using contours of potential temperature and moisture transport fields to identify specific patterns of extreme moisture transport. This was conducted using the same reanalysis products as in research task #1.

Although the GBI and PH indices effectively indicate the presence or absence of blocked conditions over Greenland, they do not distinguish intra- or inter-episode variability in the type or position of the blocking anticyclone. We therefore performed a self-organizing map (SOM; e.g., Kohonen, 1990) analysis to document the varying surface energy balance (SEB)/ surface mass balance (SMB) response to the full diversity of Greenland blocking episodes. The SOM is an artificial neural network architecture that reduces dataset dimensionality through an iterative, unsupervised classification of the input data into a user-defined number of characteristic patterns, referred to as nodes, that represent the full range of physical states present in the record (Kohonen, 1990; Miljković, 2017; Reusch et al., 2005; Sheridan & Lee, 2011). For climatological applications, the SOM is typically organized into a two-dimensional array of nodes where, as a feature of the iterative learning process, neighboring nodes are more similar than distant nodes and the corner nodes represent opposing extremes within the record (Hewitson and Crane, 2002; Kohonen, 1990; Sheridan and Lee, 2011; Tedesco and Fettweis, 2020). We utilized the SOM to classify daily ERA5 500 hPa geopotential height data for all days occurring during identified JJA blocking episodes. The geopotential height data were remapped to a 100 km EASE2 grid (Brodzik et al., 2012, 2014) using bilinear interpolation prior to the SOM analysis to ensure that all latitudes were given equal weight during the SOM training process. After visually examining multiple node configurations, we proceeded with a 4x3 SOM array due to its ability to preserve and clearly present the primary Greenland blocking configurations while limiting the number of low-frequency nodes. As a product of the SOM analysis, each blocking episode day is assigned a best matching unit (BMU) indicating the node (e.g., class) to which it is assigned in the classification process. We display the synoptic setting and attendant surface conditions that characterize each node by compositing daily values of relevant variables by common BMU assignment.

To quantify GrIS surface impact, we examined the SEB and SMB response as represented by the Regional Climate Model, Modèle Atmosphérique Régional (MAR). MAR is fully coupled to a one-dimensional surface-atmosphere energy and mass transfer scheme that employs a multilayered snowpack model that accounts for changes in surface albedo due to snow metamorphism and has been extensively verified over the GrIS (e.g., Fettweis et al., 2005, 2017; Lefebre et al., 2005). It is therefore particularly well suited for analyses of GrIS SMB. All MAR variables used here were simulated at 10 km resolution by MARv3.11 forced at the initial and lateral boundaries by ERA5 reanalysis data.

L. Wachowicz (Ph.D. candidate, UGA) led recent efforts to examine the role of El Niño on Rossby wave breaking and high-latitude moisture transport in the North Atlantic region.

Rossby wave breaking events were identified through the seasonal adaptation of the PH03 blocking methodology, as explained in Wachowicz et al. (2021), with applied additional constraints from Masato et al. (2012, 2013) to categorize each event as cyclonic or anticyclonic. Blocking is further categorized into cyclonic or anticyclonic wave breaking based on the direction of the wave break (DB), as described in (Masato et al., 2012). Starting from 0° to 359° longitude, the difference in average θ at each degree longitude was calculated. Events are considered anticyclonic (cyclonic) wave breaking if DB > 0.4 (< -0.4) for no more than 40° longitude capture synoptic scale events (Bowley et al., 2019). The threshold of DB was selected somewhat subjectively and is more restrictive than as mentioned in (Masato et al., 2012), but does not appear to significantly change the number of events identified. Unless noted otherwise, wave breaking events persisting for 3 or more consecutive days are assessed. While this is a lower temporal threshold compared to the 5-day threshold used in Masato et al. (2012), the less restrictive criterion allows for a larger sample size for compositing. Moreover, daily moisture transport during these events were calculated following Mattingly et al. (2018) and were composited with respect to different El Niño seasons, as defined by the Niño3 and Niño4 regions via the Climate Prediction Center.

As part of a visiting fellowship to the National Center for Atmospheric Research, L. Wachowicz analyzed the representation of El Niño-Southern Oscillation (ENSO)-related sea surface temperature variability on Arctic sea ice in the Community Earth Systems Model Large Ensemble (CESM LENS) (Kay et al. 2015). This effort utilized a comprehensive observational sea ice (Walsh et al. 2019) and sea surface temperature (ERSST v5) datasets for 1920-2017 in addition to historical simulations from 35 ensemble members from CESM LENS. The CESM LENS dataset contains 35 ensemble members originating from the same set of initial conditions for the period of 1920–2100 (1850–2100 for the first member). For this study, historical runs for 1920–2005 are used and concatenated with the years 2006–2017 from the RCP8.5 simulations to ensure a record of 1979–2017 to match observations, similar to the approach used by Yang and Magnusdottir (2018). This allows the use of NCAR's Climate Variability Diagnostic Package calculations of the ENSO indices, including Eastern Pacific (EP) Niño3 and Central Pacific (CP) Niño4 indices for the period of 1920–2018. To account for differences in the mean climate state across ensembles, for each ensemble, seasons of high (low) SST anomalies are those which exceed (are below) the 75th (25th) percentile compared to that ensemble's climatology, similar to observational definition of Niño (Niña) events. Atmospheric circulation composites are produced for 500 hPa anomalies for both ensemble members and ERA5 reanalysis; integrated vapor transport was also composited using ERA5 and compared to CESM LENS 850 hPa specific humidity and winds to assess moisture associated with circulation anomalies.

**Research Task #3 techniques:** An ensemble approach was used to understand how well patterns of large-scale atmospheric variability are represented in the Climate Model Intercomparison Project (CMIP)-6 models. The focus of this task was to assess how blocking was represented in a selection of historical runs within the CMIP6 suite, using composites of atmospheric moisture and energy budget components to investigate the magnitude of the impact on the Greenland ice sheet and sea ice in the NAA. For this research task, many of the metrics and techniques already described were utilized understand how summertime Arctic blocking is represented in the CMIP5 and CMIP6 output.

Finally, spurred by interest in widespread GrIS melt that occurred in July 2019, which was associated with a warm airmass that was transported along a seemingly atypical path from

its origin over Europe westward to Greenland, we also sought to identify the relative frequency of typical source regions for airmasses that have caused extensive melt within topographically defined regions of the GrIS. We defined extensive melt events occurring during the period spanning 1988–2019 as those that exceeded the 95$^{th}$ percentile of daily melt extent for at least three days. Melt extent was calculated using daily Special Sensor Microwave/Imager (SSM/I) and Special Sensor Microwave Imager/Sounder (SSMIS) brightness temperatures (Mote and Anderson, 1995; Mote, 2007).

For each of the identified melt events, we used version 4 of the Hybrid Single-Particle Lagrangian Integrated Trajectory (HYSPLIT) model, forced using Modern Era Retrospective Analysis for Research and Applications, version 2 (MERRA-2) reanalysis data (Gelaro et al. 2017), to generate 10-day back trajectories initialized at 12z on the leading day of each event. Trajectories were initialized from a 3° longitude by 1.5° latitude grid within each region. We then applied HYSPLIT's clustering algorithm separately for each region to visualize the predominant tracks of air masses that impact the GrIS during extensive melt events.

Lastly, we characterized the synoptic-scale atmospheric circulation responsible for the transport of melt-inducing airmasses from identified source regions using composites of atmospheric variables from MERRA-2 reanalysis data. Both 500 hPa geopotential height and potential temperature at the dynamic tropopause, defined as the altitude of 2 potential vorticity units (2PVU), were used to illustrate the large-scale pattern.

## Results and Discussion

Project results will be summarized under the following themes:

- Extreme blocking and moisture transport climatology in both observed atmospheric reanalysis products, and as represented in the CMIP6 model suite, using the Greenland Blocking Index
- Assessing the robustness of additional blocking metrics using observed and model data
- Greenland Blocking, Rossby wave breaking, and Greenland Ice Sheet surface melt

**Extreme blocking and moisture transport climatology using the Greenland Blocking Index:**

Extreme blocking over Greenland was found to have increased in the most recent two decades (2000-2019) when compared to the two decades prior (1980-1999), with the distribution appearing to shift right and with the extremes in the right tail shifting right as well (Fig. 5). This increase in extreme blocking agrees with others who have also studied blocking in and around Greenland (Fettweis et al., 2013; Hanna et al., 2015, 2018). Moreover, blocking was found to exhibit some interannual variability, in agreement with McLeod and Mote (2015), whereby years with frequent extreme blocking and years with scarce extreme blocking tending to cluster together (Fig. 4).

In addition, the probability of above-average IVT occurring on a day with extreme blocking is high in both summer and winter, with the highest probability of above-average IVT during an extreme GBI day in winter (Table 2). The reverse relationship was more complex, with above-average blocking likely to occur during extreme winter IVT but not extreme summer IVT. This agrees with two related studies by Rimbu et al. (2007, 2008), who showed that during high blocking frequency over Greenland the axis of maximum moisture transport extends northward to Greenland relative to the times of low blocking frequency, leading to a more active storm

track and greater moisture transport to the ice sheet. Finally, the highest values of IVT were found to occur in advance of extreme GBI, tending to lead extreme GBI by between 2.5 and 3.5 days (Fig. 6). That lead pattern was found for both summer and winter seasons. These findings are unique to this work and lead to questions about the role of moisture transport in developing or sustaining blocks over Greenland, related to questions posed by McLeod and Mote (2015b) on the role of precursor cyclones.

Results from assessing extreme blocking frequency of a CMIP6 historical run (1850-2015) indicates interannual variability of blocking throughout the model run, with an increase in the frequency of extreme blocking events in the second half of the 165-year period in winter especially (not shown). To explore blocking representation within CMIP6 more fully, a selection of historical model runs (https://www.wcrp-climate.org/wgcm-cmip/wgcm-cmip6) were used. The four historical model run included in this study were from the National Center for Atmospheric Research (NCAR), the Canadian Centre for Climate Modelling and Analysis (CCCma), the Max-Planck Institute of Meteorology (MPI), and the National Air and Space – Goddard Institute for Space Studies (NASA-GISS). These four historical model runs consist of daily forecasts from 1850 until either 2014 or 2015, each using the same variant label, which is an identifier used to distinguish each member of the ensemble. The vertical levels available were 1000, 850, 700, 500, 250, 100, 50, and 10 hPa. Specific humidity, u-direction wind, v-direction wind, and geopotential height, were used to calculate daily GBI and IVT.

Across all the institution's models for both seasons, the distributions shared similar Gaussian distributions (Fig. 7 and 8), with the NCAR model (Fig. 7a and 8a) displaying the highest GBI values for every percentile during both seasons. Also, of note was that the NASA model had the lowest values for GBI during summer and winter months (Table 5). Overall, significant variation was not expected from GBI values as geopotential height does not vary drastically within seasons. There was, however, a fairly visible difference between the summer (JJA) and winter (DJF) months' distributions (Fig. 7 and 8 respectively). Summer months had an average value of extreme GBI of 5646.75m while winter months had an average of 5371.5m. This difference can likely be explained by warmer and more consistent weather patterns during summer months. The opposite is true for weather patterns during the winter months, shown by a lower and wider distributions.

We were also interest in assessing GBI over time, from 1850 to 2015, for both winter and summer months from the model output. Summer months (JJA) displayed varying trends among all four models (Fig. 9), with the CCCma model (Fig. 9c) showing few instances of extreme GBI from 1850 to about 1960, with a very low number of 99th percentile events at all. There was, however, a feature in the CCCma summer model of a spike in all percentiles after 1980, which then plateaued until the end of the time series. This feature was not observed in any of the other institution's models. There was agreement among the NCAR (Fig. 9a), NASA (Figure 9b), and CCCma (Figure 9c) models as they all showed a slight increase in the amount of 99th percentile GBI events in the final 1/4th of the time series. Additionally, NCAR, NASA, and MPI (Figure 5d) models all show a relative maximum in the 2000-2009 time period. Similar analysis was performed for winter months (not shown here).

In considering IVT representation and trends amongst the 4 historical model runs, our ultimate goal was to see if there is a relationship between extreme blocking events over Greenland and the amount of water vapor present in the atmosphere in the model output, and how that compared to our previously completed observational study. To better understand the distribution of moisture transport during summer (JJA) and winter (DJF) months, distributions of

IVT for each were analyzed. Over all of the IVT model distributions, there was much more variation among the different models than there was between GBI distributions (not shown). This was expected as IVT is a much more variable measurement by the nature of how and what it is measuring. Moisture varies by large magnitudes sometimes from day to day, going from a largely saturated atmosphere to largely dry atmosphere. IVT is measuring the amount of moisture from these types of events.

IVT distributions from summer months (JJA) (Table 6) showed similar results to GBI (Table 5) in that, overall, values of IVT were higher in summer than in winter. This result was expected, due to higher moisture values in the atmosphere during summer months as a result of warmer air temperatures allow for greater amounts of evaporation to take place. The substantial differences present between institution's distributions of IVT may be due to the models' different resolutions, and treatment of moisture variables within the models.

Finally, lead-lag analysis was performed for both summer and winter months between extreme GBI events and above average IVT events (Fig. 10 and 11). This analysis was similar to that carried out in previous years of this project using observational data, and was aimed at exploring the potential relationship between moisture transport and extreme blocking, and identify at which time lag moisture transport either leads or lags extreme blocking. For summer months the NCAR, CCCma, and MPI models (Fig. 10a, c and d), all show a similar pattern, which consists of an increase in moisture transport for the entire 30-day period of the lead-lag while NASA (Figure 6b) remains relatively constant. For NCAR, CCCma, and MPI models, the overall increase of moisture transport over the 30-day period is most prevalent for the 90th percentile (Figure 10, blue bars). A feature that is constant throughout all models in the summer months (JJA) is that there is a relative maximum of moisture transport 15 days before and 15 days after day zero of the extreme GBI event in every model, increase seen in 3 of the 4 models, and is indicative of moisture transport being delayed in its arrival from the initial GBI event onset in summer months (JJA).

The lead-lag relationship between IVT and GBI during winter months (DJF; Fig. 11) shows contrasting results to that of the summer months. Specifically, the NASA, CCCma, and MPI (Fig. 11b, c and d) models all show a significant decrease in IVT values from 15 days before an extreme GBI event. For these three models, the pattern stays fairly constant after the extreme GBI event, only increasing slightly immediately after the extreme GBI event. This small increase however, is not insignificant as it suggests that winter extreme blocking events have a more immediate impact on moisture transport. Also of note, these 3 models show the most variation among the 95th and 97th percentile GBI events while 90th and 99th percentile events remain relatively constant. The NCAR model (Fig. 11a) displays a small tri-model peaks for the overall level of above average IVT occurrence. The decreasing trend observed in 3 out of 4 of the models, most significantly from CCCma and MPI, indicates that moisture transport leads blocking events over Greenland in the winter months.

**Assessing the robustness of additional blocking metrics using observed and model data:**
In all seasons the TM-based metric consistently underestimates days with blocking per season compared to both the PH-based metrics (Fig. 13). Figure 13 shows the frequencies of the TM index (blue), and original and modified variations of the PH index (purple and magenta, respectively). Both versions of the PH index likewise remain consistent in capturing blocking over Greenland for the transitional seasons but show differing frequencies of blocking in both DJF and JJA, with the greatest difference between the two metrics in JJA. In particular, for DJF

the original PH index results in higher blocking frequency when compared to the modified variation of the index. In JJA, the modified index results in a higher seasonal blocking frequency when compared to the original PH metric.

Both PH metrics show increases in blocking frequency corresponding with the trends shown in the GBI during the period of 1990 onward for JJA (Fig. 13, purple and magenta lines). Notably, both the TM and PH indices indicate decreasing blocking in SON. Table 3 shows that based on a Mann-Kendall test to assess the presence of trends, negative trends exist during the SON season across all metrics, with a significantly decreasing trend in the TM metric ($p < 0.05$). The raw GBI anomaly, however, indicates positive trends in all seasons, except SON, with these trends being significant in JJA (Fig. 13). Furthermore, for JJA, the original PH index suggests a negative trend, whereas the modified PH index is more consistent with other indices by suggesting a positive trend. Across the different metrics, with the exception of the raw GBI anomalies, decreasing trends in blocking frequency, although not statistically significant, are present for both DJF and SON (Fig. 13 and Table 3).

In general, the different blocking metrics are relatively consistent in identifying abnormally high or low blocking seasons, particularly in DJF and MAM (Fig. 14). As also shown in Figure 13, discrepancies exist between the TM- and PH-based indices for JJA and SON regarding blocking frequency, suggesting either the TM index may underestimate, or the PH-based indices are overestimate total blocking frequency over Greenland. For SON, there are anomalously low blocking frequencies compared to both the GBI and PH indices during the period of 1990-2005. It is possible that this underestimation of blocking during this period may be contributing to the statistically significant decreasing trend in SON blocking when using the TM metric, although this may warrant further investigation. There are inconsistencies between the different metrics during JJA that are prevalent during 2007-2012. In particular, the GBI is consistently higher during this period, which may be because of a possible overestimation of blocking by this metric or underestimation of the other metrics.

Differences between TM-based blocking compared to the PH-based metrics and GBI are also present in JJA (Fig. 14) and are particularly interesting in the context of individual events. In July 2012, for instance, the Greenland ice sheet experienced record surface melting (Nghiem et al., 2012), where much of this melting was aided by consistently strong anticyclone activity over the region (Tedesco et al., 2013). In Figure 14, JJA of 2012 shows blocking anomalies of over 2.5 standard deviations above average, according to the raw GBI, GBI-Z, and both PH indices. We also note the apparent underestimation of PH-based blocking compared to the GBI and TM indices during the period of 1995 to 2003 (Fig. 14). This period of time further illustrates, much like the period of 1990 to 2005 for SON, that no single blocking metric may fully capture Greenland blocking.

Finally, we apply a 5-year running mean to the anomalies from Figure 14 similar to that of Hanna et al. (2018), and those are shown in Figure 15. There is consistency across metrics for DJF and MAM in terms of trends in the 5-year mean; however, the raw GBI anomalies and GBI-Z for DJF are significantly increasing (Table 4). A decreasing trend is also shown in SON (Fig. 15), where these trends are considered significant for the raw GBI anomalies and the TM index (Table 4). Most notably, the significant increasing trends in blocking are present in JJA for all metrics, except the original PH index (Table 4). Even though the trends are considered significant, it appears that the GBI-based metrics (including raw and both adjusted methods) show a stronger increase in blocking since the mid-1990s, which is consistent with findings from Hanna et al. (2018).

Preliminary results comparing Arctic blocking and seasonal EKE in the different models suggests both metrics appear to improve in representation from CMIP5 to CMIP6 when compared to the ERA5. In both the CMIP5 and CMIP6 versions of each model, the areas of prominent blocking remain consistent across models; however, the frequency of blocking across all models shows more variability in these regions (not shown). Temporal frequencies of blocking during the 1979-2004 period indicate that CMIP6 models better estimate blocking closer to ERA5 observations than the CMIP5 models (Fig. 16a). Unlike the Pelly and Hoskins (2003) and methods described in Masato et al. (2013) which both use EKE to designate a central blocking latitude, the use of a constant latitude overestimates JJA blocking compared to ERA5. Interestingly, when looking at the spatial variability of maximum JJA EKE, large variability exists in what would be the central blocking latitude (i.e., Pelly and Hoskins, 2003) for the CMIP5 models when compared to ERA5; this central blocking latitude remains far more consistent across models and closer to observations in CMIP6 (Fig. 16b). The inclusion of EKE-defined central blocking latitude remains future work.

Our analysis of airmass source regions suggests that the eastern origin of the 2019 melt event was indeed atypical, with the majority of airmasses associated with extensive melt of the GrIS originating over North America and the western Atlantic. We also found that airmasses which originate over Europe and the eastern Atlantic are more frequently associated with extensive melt in the eastern and northern regions of the GrIS than with extensive melt in regions along the western face of the ice sheet. Examination of both potential temperature at 2PVU and composites of 500 hPa geopotential height suggest that cyclonic wave breaking plays a critical role in facilitating airmass transport from Europe, while transport from the west is more commonly a product of enhanced ridging centered over eastern Greenland.

**Greenland Blocking, Rossby wave breaking, and Greenland Ice Sheet surface melt:** When considering the impact of blocking on the Greenland ice sheet (GrIS), first we generated a reference climatology of the impact of Greenland blocking on GrIS surface conditions by focusing on instances of four or more consecutive days where both the Greenland blocking index (GBI) and the Pelly and Hoskins index (PH03) identify large-scale blocking. We interpreted these blocking episodes of overlap between GBI and PH03 as a conservative definition that requires a reversal of the meridional potential vorticity gradient that is accompanied by a persistent, anomalous anticyclone over Greenland. On average, these GBI-PH03 overlap blocking episodes are characterized by an upper-level ridge with strongest high-pressure anomalies centered over southwest Greenland. These anticyclonic conditions are met by widespread above-normal surface air temperature with anomalies that are maximized over high elevations, particularly in northern Greenland. Figure 17 shows the effect of blocking on surface melt as represented by MAR at relevant DoD sites: Thule, Camp Century, Dye-2 and Summit Stations. Blocking episode days are associated with an increased frequency of melt relative to non-blocking days at all four locations and it is clear that the magnitude of meltwater production at Thule and DYE-2, in particular, is greater during blocked conditions than when blocked flow is not present.

A key objective of our project on this topic has been to consider how using different blocking metrics will affect our understanding of surface processes. In pursuit of this objective, we documented the synoptic patterns identified by two independent blocking metrics using SOMs, then contrasted the GrIS surface response between those patterns. Doing so also allowed us to identify the distinct impacts of differing blocking patterns and their temporal variability at

DoD-relevant locations. In its application here, the self-organizing map (SOM) was used to classify events into 3 key blocking types: (1) a high-amplitude Omega block, (2) a lower-amplitude, stationary summer ridge (SR), and (3) a cyclonic wave breaking pattern (CWB) (Fig. 18).

Relative to all blocking episodes, cyclonic wave breaking patterns produce more melt in northeast Greenland, summer ridge patterns produce more melt over the southern ice sheet, and Omega blocks produce more melt across the northern ice sheet (Figure 19). Focusing on the radiative and turbulent heating terms contributing to these melt patterns (not shown), CWB nodes exhibits a west–east dipole in shortwave radiation (SWD) that is primarily focused over northern Greenland with negative anomalies to the west and positive anomalies to the east (not shown), while the composite anomalies for longwave radiation (LWD) show an inverse pattern. This is consistent with IVT composites which show moisture delivery through the Davis Strait after wrapping anticyclonically around the southern tip of Greenland from its origin over the northeast Atlantic (not shown). The resulting onshore moisture advection over the northwest GrIS is favorable to cloud formation that would decrease SWD and increase LWD. Conversely, the cross-barrier IVT over northern Greenland is conducive to lee-side subsidence in northeast Greenland that would increase SWD and reduce LWD. Anomalous positive sensible head flux is most extensive during CWB patterns. This is particularly true in northeast Greenland, where above-normal SHF extends to elevations above 3000m, and southwest Greenland, where above-normal sensible heat flux (SHF) extends to above 2500m.

The radiative terms associated with SR patterns exhibit a similar west–east dipole as observed during CWB patterns. However, as the ridge builds and migrates westward, below-normal (above-normal) SWD (LWD) extends across northwest Greenland as the new positioning of the ridge allows for increased moisture transport through the Davis Strait. Coincidentally, SWD and SHF increases along the southeast margin of the ice sheet as the northwesterly flow downstream of the ridge axis generates downslope flow.

Again, like SR and CWB patterns, there is a west–east oriented dipole in the anomalous radiative forcing associated with moisture delivery to northwest Greenland through the Davis Strait when Omega blocking is centered over eastern Greenland. As the ridge axis migrates west, southerly IVT to northwest Greenland gives way to northerly IVT over northern Greenland. Consequently, the dipole rotates clockwise such that negative SWD anomalies are centered over the northern ice sheet and positive SWD anomalies occupy the southern ice sheet, while the inverse pattern is apparent for LWD. Thus, there is a similar clockwise rotation in the surface radiative terms as both Omega and SR blocks progress westward, although this rotation is much more pronounced for Omega blocks. Focusing on the non-radiative forcing, above-normal SHF during Omega blocking is greatest in the west-central ablation zone.

The magnitude and extent of surface melt during CWB patterns is highly variable between individual nodes; however, nodes 1–3 show that they consistently enhance meltwater production (ME) in the eastern ablation zone relative to all blocking episode days (Figure 19). This is consistent with the eastern origin of the blocking anticyclone (Figure 18) and appears to be driven by greater SWD and enhanced SHF. Relative to all blocking episodes, SR patterns generate greater surface melt in southern Greenland, where the northernmost extent of the strongest melt anomalies closely tracks the position of the block. Melt anomalies are greatest in the southwest ablation zone, including strong positive anomalies around DYE-2, where SR blocking is associated with increased LWD and enhanced SHF. Omega blocking brings greater surface melt to northern Greenland than other blocking episodes. Nodes 7 and 8 (Figure 19), in

particular, show enhanced surface melt extending to >2000m in northwest Greenland, including areas encompassing Thule and Camp Century. Conversely, Omega blocks generally produce less meltwater than other blocking episodes across the southern ice sheet. The strongest melt during Omega blocking is largely aligned with locations of above-normal LWD above 1000m and enhanced SHF at below 1000m.

We examined differences in long-term trends between each blocking type and investigated interannual variability in Greenland blocking patterns by documenting the relationship with the North Atlantic Oscillation (NAO) (Figure 20). A least-squares linear regression shows that Omega blocking exhibits the strongest relationship with the NAO, with $p < 0.01$ and $R2 = 0.34$, and the strongest long-term trend, with a modeled increase of 0.22 blocking episode days per year from 1979–2019. These results indicate that the recent trend in summer Greenland blocking was largely driven by an increase in Omega patterns. Recent modeling efforts have demonstrated that accelerated SMB decline has been driven by a disproportionate increase in surface melt and runoff from northcentral and northwestern drainages of the ice sheet (Noël et al., 2019). Furthermore, these same efforts show that augmented runoff from northern Greenland is a consequence of enhanced longwave cloud radiative forcing over the northern ice sheet in recent decades that has caused the rapid ablation of snow cover and exposure of the underlying glacial ice at lower elevations while also reducing diurnal variability in surface temperature and thus meltwater refreeze at higher elevations (Noël et al., 2019). We show that Omega blocks, specifically, enhance LWD and generate greater surface melt over the northern ice sheet than other blocking types which, in turn, depresses the surface albedo and increases absorbed shortwave radiation. Thus, our results suggest that the increase in Omega patterns since the turn of the century has played a central role in augmenting GrIS mass loss. Furthermore, GBI exhibited a relative bias toward Omega patterns, which may help explain why it has measured stronger trends in summer Greenland blocking than other blocking metrics.

When focusing on our analysis on North Atlantic Rossby wave breaking activity explicitly, we note a discernable difference in CWB versus AWB activity. In particular, although blocking with wave breaking is a relatively infrequent phenomenon, with typically fewer than 30 separate events per year, we note the presence of more frequent CWB over the western portion of the North Atlantic basin, particularly in warm seasons (March-May, June-Aug) (not shown). A 3-year running mean is applied to the wave breaking frequency anomalies (Figure 21), with results from a Mann-Kendall test indicating an increase in AWB days in SON and CWB days in JJA ($p < 0.05$). These trends complement findings from Wachowicz et al. (2021), who noted potential decreases in SON Greenland blocking activity and increases in JJA Greenland blocking, though the identification of these trends is sensitive to how Greenland blocking is identified.

Tropical variability, including variability in the manifestation of El Niño events, play a strong role in modulating North Atlantic climate. In JJA with positive SST anomalies, the IVT within the North Atlantic AWB region is less than 75% of all documented AWB events (Figure 22). IVT is significantly reduced in this region for the Niño4 events compared to Niño3, suggesting that JJA AWB under El Niño4 conditions results in less moisture transport compared to AWB under El Niño3 conditions. On the other hand, CWB events show increased moisture transport within the wave breaking region that exceeds 150% compared to all CWB for El Niño4 events. This enhanced IVT within the CWB region is significantly higher than the El Niño3 events. These findings suggest that El Niño4 SST anomalies may result in increased moisture transport during CWB events in the North Atlantic during the summer. Given the hypothesized

shift in El Niño events towards a CP/Niño4 -type of event (e.g., Freund et al. 2019), results here suggest a likelihood of enhanced moisture transport in the North Atlantic region and leaving the observed and projected diabatic heating impact on blocking development in climate models and its surface melt consequences up for debate.

In analyzing the impact of low-latitude processes, such as ENSO, on Arctic sea ice concentration (SIC) and area (SIA), we found that the Canadian Archipelago displays strongest sensitivity in SIC and SIA to tropical Pacific SST anomalies when they originate from the EP region from about late spring to summer (April-July, not shown). This response is not readily apparent for the CP anomalies, despite both ENSO regions indicating a negative correlation in sea ice. Both the Beaufort Sea and Canadian Archipelago regions have less springtime, and possibly early summer, sea ice under possible El Niño conditions more generally (i.e., positive SST anomalies). In particular, sea ice in these regions is likely most impacted by the SST anomalies originating from the Niño3 region, which may further influence the summertime sea ice response.

Figure 23 shows the correlation coefficients of JJA SST anomalies and lagged SIA time series. When considering no lag (i.e., JJA SIA), positive correlations between SIC and SSTs for the Niño 4 index exist near the Beaufort Sea into the Canadian Archipelago regions, extending into the Central Arctic, while these positive correlations are limited to the Canadian Archipelago for the Niño3 SSTs anomalies. SIC from July–December is positively correlated (correlations exceeding 0.4) to the CP index in the Canadian Archipelago region compared to the EP SST anomalies. This is consistent with Hu et al. (2016), who showed that a CP-type of El Niño will inhibit summer Arctic warming and reduce sea ice loss in this region. Additionally, the prominent positive correlations (exceeding 0.3) in the Central Arctic are prevalent for both ENSO indices, particularly for June–October. However, these significant correlations persist longer into the autumn and early winter (October-November) for CP ENSO events.

Summer months generally exhibit weaker atmospheric ENSO signals in the sea ice compared to the winter (Figure 24). Most pronounced is enhanced moisture transport of 20% or greater in the North Atlantic and northern portion of the Canadian Archipelago under Niño4 conditions compared to Niño3 conditions. These atmospheric responses are qualitatively similar up to 2 months later, with minor variation in the placement of high/lows. Similarly, above-normal moisture transport occurs in northwestern and coastal Greenland and Barents-Kara seas under Niña4 conditions compared to Niña3, due to the placement of an upper-level ridge over the region. Given the northerly 850 hPa winds around the Canadian Archipelago region, under the Niño4/Niña4 conditions it is possible that the positive correlations exhibited between the sea ice and Niño4 SST anomalies are related to circulation patterns conducive to either ice import into the region or is the lagged result of lack of sea ice loss under JFM Niño4/Niña4 conditions.

In examining these relationships in CESM LENS, we note no significant correlation between ENSO and sea ice, which we attribute to weak circulation anomalies (and associated moisture) in the simulations (not shown). While this analysis considers CESM, version 1, Gettleman et al. (2019) show significant improvements in clouds and related feedbacks in CESM version 2 from CESM version 1. Documented changes in Arctic liquid clouds, related precipitation, and surface energy fluxes in CESM2 may better simulate the sea ice-atmosphere interface and have implications on sea ice (DuVivier et al., 2020; McIlhatten et al. 2020). This consideration of the representation of Arctic cloud processes likewise leaves uncertainty for historical and projected GrIS SMB/SEB estimates in GCM simulations going forward.

## Conclusions and Implications for Future Research:

The goal of this work was to understand and quantify the role of large-scale, low-frequency atmospheric circulation anomalies and moisture transport on the ice climate system of the North Atlantic sector of the Arctic (North Atlantic Arctic, NAA). This work was motivated by recent changes in low-frequency atmospheric circulation in the NAA and their influence on sensible heat and moisture advection from the mid-latitudes into the Arctic, the surface energy budget over the Greenland Ice Sheet (GrIS) and adjacent sea ice, resulting in unprecedented melt and freshwater runoff events. Impacts of such changes have significant implications on DoD infrastructure and operations in the NAA, and have the potential to disrupt mission training at DoD installations across the region.

To anticipate and reduce the negative consequences of these extreme events, and to assess the impact of large-scale atmospheric circulation and moisture transport on high-latitude DoD operations and installations in the North Atlantic Sector of the Arctic, this project's research objectives were to; 1) quantify the contributions from large-scale atmospheric circulation and moisture transport to ice melt events across multiple time scales, 2) to understand how atmospheric blocking and Rossby wave breaking impact, and are impacted by, the transport of moisture from mid-latitudes into the NAA, and 3) to investigate the role of this moisture advection in altering radiative and turbulent fluxes, winds, precipitation, surface melting, and snow accumulation in the NAA.

Objective 1 was largely achieved by the development of a Greenland blocking and moisture climatology using both atmospheric reanalysis products and climate model output. Key findings relating to these objectives include the following:

- Extreme atmospheric flow blocking over Greenland has increased in the period 2000-2019 compared to 1980-1999. The increase has been seen in both winter (December-February) and summer (June-August). Moreover, blocking was found to exhibit some interannual variability, in agreement with McLeod and Mote (2015), whereby years with frequent extreme blocking and years with scarce extreme blocking tending to cluster together (Fig. 4).
- Atmospheric moisture transport is associated with extreme flow blocking in and around Greenland in both seasons. Above-normal moisture transport (quantified by integrated vapor transport, IVT) over Greenland seems to lead, rather than lag, extreme blocking, by an average of three days (Fig. 6). These findings are unique to this work and lead to questions about the role of moisture transport in developing or sustaining blocks over Greenland, related to questions posed by McLeod and Mote (2015b) on the role of precursor cyclones.
- Greenland blocking calculated from the Greenland Blocking Index (GBI) shows an increase in blocking for DJF and MAM with significant increases in JJA; once detrended, the GBI, Tibaldi and Molteni (TM) and Pelly and Hoskins (PH) indices suggest an insignificant decrease in blocking during SON and DJF and increase in blocking during MAM and JJA. However, the use of one particular metric over another may limit the assessment of individual case studies (Fig. 14).
- The use of a constant latitude in identifying instantaneous Arctic blocking in the CMIP5 and CMIP6 models has limitations regarding the frequency of blocking more so than the preferred regions of blocking. Despite this, CMIP6 models appear to better represent blocking conditions over the 1979-2004 period when compared to CMIP5. Furthermore, the inclusion of eddy kinetic energy (EKE) in defining blocking may improve current Arctic blocking climatologies in climate models (Fig. 16).

In terms of objective 2, Rossby wave breaking and its relationship to Greenland blocking and moisture transport into the NAA, and objective 3, the role of this moisture advection in altering the surface energy balance and subsequent influence in melt events, some key findings included:

- Relative to all blocking episodes, summer ridge patterns produce more melt over the southern ice sheet, Omega blocks produce more melt across the northern ice sheet, and cyclonic wave breaking patterns produce more melt in northeast Greenland (Fig. 18 and 19).
- Distinct mechanisms of melt production for each blocking type include: lower-amplitude, summer ridge patterns direct onshore moisture transport into southwest Greenland, generating above-normal longwave downward radiation and increased sensible heat flux that aligns with relatively more melt over the southern ice sheet than other blocking types; cyclonic wave breaking patterns produce an apparent foehn effect where cross-barrier flow generates above-normal incoming shortwave radiation and enhanced sensible heat flux that accompanies relatively more melt over northeast Greenland; and high-amplitude, Omega blocking directs onshore flow over the northwestern and northern coastlines, generating above-normal longwave downward radiation that aligns with relatively greater melt across the northern GrIS. Moreover, the location and frequency of Greenland blocking may impact heat and moisture transport near Thule. This poses significant threat on Thule's infrastructure, as increased liquid precipitation and warmer temperatures will act to accelerate permafrost melt.
- Omega blocking patterns have increased more than other blocking types. Given the failure of global climate models to resolve the overall increase in Greenland blocking (Hanna et al. 2018; Slater et al. 2020), if the increase in Omega blocking were to continue, it would likely result in the underestimation of future GrIS melt. This is particularly true for the northern ice sheet where Omega blocks produce more melt than other blocking types, which has important implications for surface mass loss over Camp Century and runoff near Thule.
- The number of days in the North Atlantic exhibiting cyclonic wave breaking (CWB) characteristics in JJA have significantly increased (Fig. 21), which corresponds to observed increased Greenland blocking conditions and increased moisture transport. This is important considering our findings suggest higher IVT under CWB conditions, especially in JJA. Higher IVT values are present during Central Pacific El Nino when compared to EP El Nino, further demonstrating tropical influences of NAA hydroclimatology.
- Summer sea ice in the Canadian Archipelago and Central Arctic regions appears most sensitive to the Central Pacific El Niño, resulting in less sea ice loss. While this may be due to springtime sea ice-ENSO connections, the increase in moisture transport during Central Pacific ENSO events within the region and its impact on the sea ice warrants further investigation (Fig. 23). The connection between these mechanisms is not prevalent in CESM LENS, and should be investigated in CESM2 and other CMIP6 models.

In summary, the results of this project have shown that it is critical to understand patterns of atmospheric circulation in the high latitudes, including when those patterns are disrupted, which happens during blocking. We found that blocking has the potential to significantly impact the Greenland ice sheet. It can provoke rapid melting and runoff, depending on the location where the blocking pattern sets up. We also found trends toward more periods of extreme

blocking in the most recent 20 years, and will continue analyzing whether that trend appears in sophisticated climate model predictions of the coming decades.

More work is needed on blocking's impacts on specific sensitive DoD infrastructure and operations in Greenland, including and specifically at Thule Air Base, which is now home to critical operations of USSF Delta 2 (space situational awareness) and Delta 4 (spaceborne missile detection) groups. This work will be explored in an extension of this project, in which we seek to assess the climate security of northwest Greenland by investigating and understanding trends in past and expected future climate of the region. We will leverage the findings of this project, transitioning basic research to support critical DoD base infrastructure integral to current and future Space Force endeavors. Specifically, we will focus on Thule Air Base and the surface conditions that adversely affect base operations and the surrounding region, in addition to improving spatial representation in global Earth system models.

# Tables

**Table 1.** Frequencies of extreme GBI events (days with GBI index in the 90th, 95th, 97th, or 99th percentiles) by year: 1980-1999 and 2000-2018, for winter (DJF) and summer (JJA) months. From Barrett et al. 2020.

| Percentile of GBI Values | Season | Total Occurrences | Percent of Occurrences | |
|---|---|---|---|---|
| | | | 1980-1999 | 2000-2018 |
| 90th | DJF | 358 | 41.9% | 58.1% |
| | JJA | 368 | 28.0% | 72.0% |
| 95th | DJF | 179 | 38.0% | 62.0% |
| | JJA | 184 | 25.5% | 74.5% |
| 97th | DJF | 107 | 30.8% | 69.2% |
| | JJA | 110 | 23.6% | 76.4% |
| 99th | DJF | 36 | 19.4% | 80.6% |
| | JJA | 37 | 16.2% | 83.8% |

**Table 2.** Seasonal likelihood of above average IVT days within varying extreme GBI thresholds (top). Seasonal likelihood of above average GBI days within varying extreme IVT thresholds (bottom). From Barrett et al. 2020.

| | DJF | | | JJA | | |
|---|---|---|---|---|---|---|
| GBI Percentile | Days with high IVT | Total days | Percent (%) | Days with high IVT | Total days | Percent (%) |
| 90th | 281 | 358 | 78.5% | 233 | 368 | 63.3% |
| 95th | 158 | 179 | 88.3% | 136 | 184 | 73.9% |
| 97th | 98 | 107 | 91.6% | 80 | 110 | 72.7% |
| 99th | 32 | 36 | 88.9% | 28 | 37 | 75.7% |
| | DJF | | | JJA | | |
| IVT Percentile | Days with high GBI | Total days | Percent (%) | Days with high GBI | Total days | Percent (%) |
| 90th | 225 | 355 | 63.4% | 170 | 368 | 46.2% |
| 95th | 119 | 177 | 67.2% | 88 | 184 | 47.8% |
| 97th | 73 | 106 | 68.9% | 54 | 110 | 49.1% |
| 99th | 29 | 35 | 82.9% | 17 | 37 | 46.0% |

**Table 3.** Results from an original Mann-Kendall test for presence of trends, using standardized seasonal blocking frequency anomalies. Result statistics include the p-value (p), normalized test statistic (z), Kendall Tau (tau), the Mann-Kendall score (s), the variance of the MK score (var_s), and sen's slope (m). Trends are considered statistically significant for $p < 0.05$ and are indicated in bolded text.

| | | GBI | GBI-Z | PH | PH_seasonal | TM |
|---|---|---|---|---|---|---|
| SON | p | 0.8846 | 0.0999 | 0.3504 | 0.4375 | **0.0230** |
| | z | -0.1452 | -1.6452 | -0.9338 | -0.7764 | -2.2734 |
| | tau | -0.0175 | -0.1849 | -0.1053 | -0.0877 | -0.2537 |
| | s | -13 | -137 | -78 | -65 | -188 |
| | var_s | 6833.6667 | 6833.6667 | 6800.0000 | 6795.0000 | 6766.0000 |
| | m | -0.0900 | -0.8116 | -0.0952 | -0.0833 | -0.1935 |
| DJF | p | 0.5136 | 0.5453 | 0.9614 | 0.7991 | 0.1671 |
| | z | 0.6532 | -0.6048 | -0.0484 | -0.2546 | -1.3815 |
| | tau | 0.0742 | -0.0688 | -0.0067 | -0.0297 | -0.1552 |
| | s | 55 | -51 | -5 | -22 | -115 |
| | var_s | 6833.6667 | 6833.6667 | 6823.6667 | 6804.6667 | 6809.0000 |
| | m | 0.4213 | -0.4825 | 0.0000 | 0.0000 | -0.1786 |
| MAM | p | 0.3838 | 0.7348 | 0.5853 | 0.5940 | 0.7253 |
| | z | 0.8710 | 0.3387 | 0.5456 | 0.5330 | -0.3514 |
| | tau | 0.0985 | 0.0391 | 0.0621 | 0.0607 | -0.0405 |
| | s | 73 | 29 | 46 | 45 | -30 |
| | var_s | 6833.6667 | 6833.6667 | 6802.6667 | 6814.3333 | 6810.0000 |
| | m | 0.5861 | 0.1912 | 0.0769 | 0.1071 | -0.0500 |
| JJA | p | **0.0119** | 0.1755 | 0.2700 | 0.2252 | 0.8078 |
| | z | 2.5161 | 1.3548 | -1.1031 | 1.2129 | 0.2433 |
| | tau | 0.2821 | 0.1525 | -0.1242 | 0.1363 | 0.0283 |
| | s | 209 | 113 | -92 | 101 | 21 |
| | var_s | 6833.6667 | 6833.6667 | 6806.0000 | 6797.6667 | 6759.0000 |
| | m | 1.0656 | 0.5374 | -0.1111 | 0.1429 | 0.0000 |

**Table 4**. Same as Table 5, but for using the 5-year running mean of seasonal standardized anomalies. Trends are considered statistically significant for p <0.05 and are indicated in bolded text.

| | | GBI | GBI-Z | PH | PH seasonal | TM |
|---|---|---|---|---|---|---|
| SON | p | 0.1475 | 0.0736 | 0.1216 | 0.2272 | **0.0001** |
| | z | 1.4485 | -1.7894 | -1.5481 | -1.2075 | -3.9358 |
| | tau | 0.1731 | -0.2134 | -0.1849 | -0.1445 | -0.4672 |
| | s | 103 | -127 | -110 | -86 | -278 |
| | var_s | 4958.3333 | 4958.3333 | 4957.3333 | 4955.3333 | 4953.3333 |
| | m | 0.0099 | -0.0154 | -0.0109 | -0.0108 | -0.0348 |
| DJF | p | **0.0054** | 0.4954 | 0.1640 | 0.2112 | 0.4774 |
| | z | 2.7835 | 0.6817 | 1.3917 | 1.2502 | 0.7105 |
| | tau | 0.3311 | 0.0824 | 0.1664 | 0.1496 | 0.0857 |
| | s | 197 | 49 | 99 | 89 | 51 |
| | var_s | 4958.3333 | 4958.3333 | 4958.3333 | 4954.3333 | 4951.6667 |
| | m | 0.0247 | 0.0076 | 0.0136 | 0.0141 | 0.0064 |
| MAM | p | 0.0995 | 0.5136 | 0.3063 | 0.2441 | 0.5135 |
| | z | 1.6474 | 0.6533 | 1.0229 | 1.1648 | 0.6534 |
| | tau | 0.1966 | 0.0790 | 0.1227 | 0.1395 | 0.0790 |
| | s | 117 | 47 | 73 | 83 | 47 |
| | var_s | 4958.3333 | 4958.3333 | 4954.3333 | 4956.3333 | 4956.3333 |
| | m | 0.0170 | 0.0070 | 0.0077 | 0.0094 | 0.0033 |
| JJA | p | **0.0000** | **0.0000** | 0.7545 | **0.0000** | **0.0097** |
| | z | 5.5386 | 4.3172 | 0.3127 | 4.1330 | 2.5864 |
| | tau | 0.6571 | 0.5126 | 0.0387 | 0.4908 | 0.3076 |
| | s | 391 | 305 | 23 | 292 | 183 |
| | var_s | 4958.3333 | 4958.3333 | 4950.3333 | 4957.3333 | 4951.6667 |
| | m | 0.0589 | 0.0402 | 0.0019 | 0.0268 | 0.0140 |

**Table 5:** Greenland Blocking Index (GBI) height values (in m) for 90$^{th}$, 95$^{th}$, 97$^{th}$, and 99$^{th}$ percentiles for summer and winter months from 4 CMIP6 historical model runs. The 4 models included were the National Center for Atmospheric Research (NCAR), the National Air and Space – Goddard Institute for Space Studies (NASA-GISS), the Canadian Centre for Climate Modelling and Analysis (CCCma) model, and the Max-Planck Institute of Meteorology (MPI). Each historical model run spanned from 1850-2015.

| GBI | JJA | | | | DJF | | | |
|---|---|---|---|---|---|---|---|---|
| Percentile | NCAR | NASA | CCCma | MPI | NCAR | NASA | CCCma | MPI |
| 90th | **5637** | *5591* | 5618 | 5604 | **5344** | *5229* | 5285 | 5334 |
| 95th | **5664** | *5619* | 5641 | 5628 | **5394** | *5278* | 5328 | 5378 |
| 97th | **5681** | *5636* | 5657 | 5643 | **5424** | *5312* | 5357 | 5408 |
| 99th | **5711** | *5665* | 5682 | 5671 | **5637** | *5371* | 5407 | 5458 |

**Table 6**: As in table 5 for Integrated Vapor Transport values (in kg m$^{-1}$ s$^{-1}$).

| IVT | JJA | | | | DJF | | | |
|---|---|---|---|---|---|---|---|---|
| Percentile | NCAR | NASA | CCCma | MPI | NCAR | NASA | CCCma | MPI |
| 90th | **290** | 196 | 165 | *157* | **208** | 102 | *69* | 101 |
| 95th | **339** | 235 | 178 | *172* | **276** | 154 | *79* | 113 |
| 97th | **372** | 266 | 186 | *181* | **332** | 202 | *87* | 121 |
| 99th | **434** | 337 | 202 | *201* | **466** | 323 | *101* | 140 |

# Figures

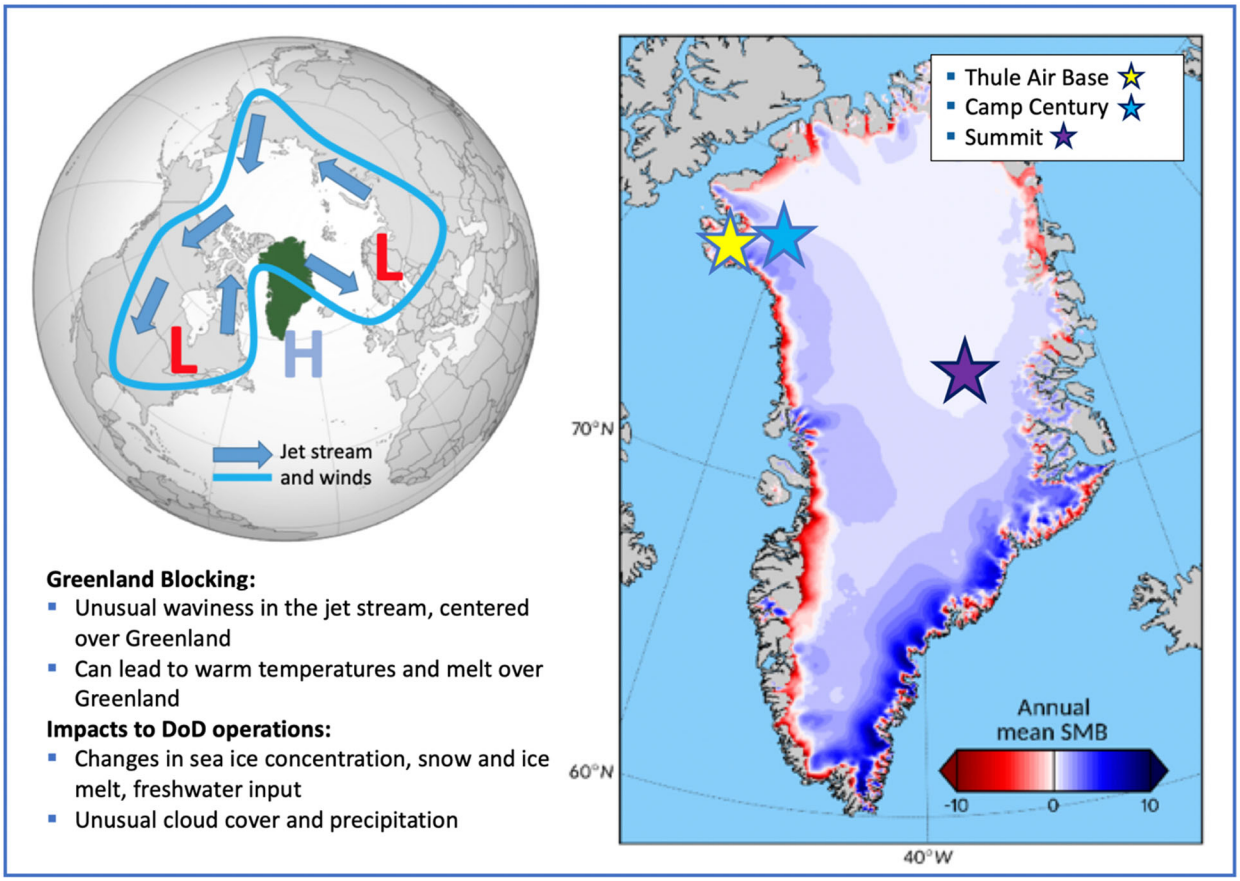


**Figure 1:** Schematic highlighting both the spatial extent and physical implications of Greenland Blocking (left), and the implications for high-latitude Department of Defense (DoD) operations (right).

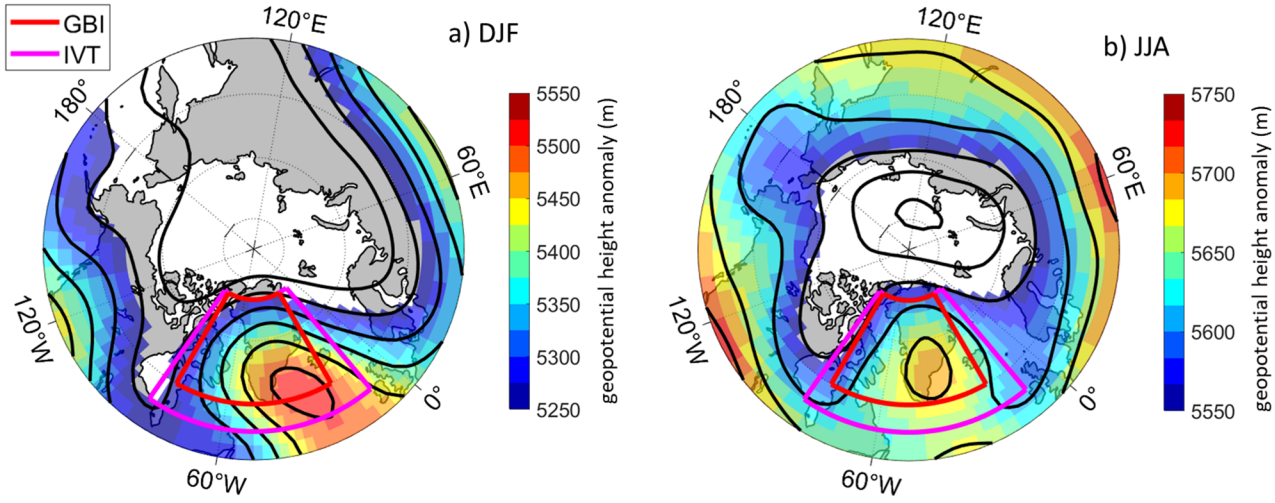


**Figure 2**: Height field (in m) at 500-hPa on days in (a) DJF and (b) JJA when the NOAA Greenland Blocking Index (GBI) was above the 95$^{th}$ percentile. Both shading and contours indicate mean heights, and contours are drawn between 5200 and 5800 m at 60-m increments. Red boxed region indicates the spatial domain averaged to calculate the NOAA GBI index, and the magenta boxed region indicates the domain used to calculate integrated vapor transport (IVT) from the ERA-Interim reanalysis. Note the color scale is different in panel (a) and (b). Figure from Barrett et al. 2020.

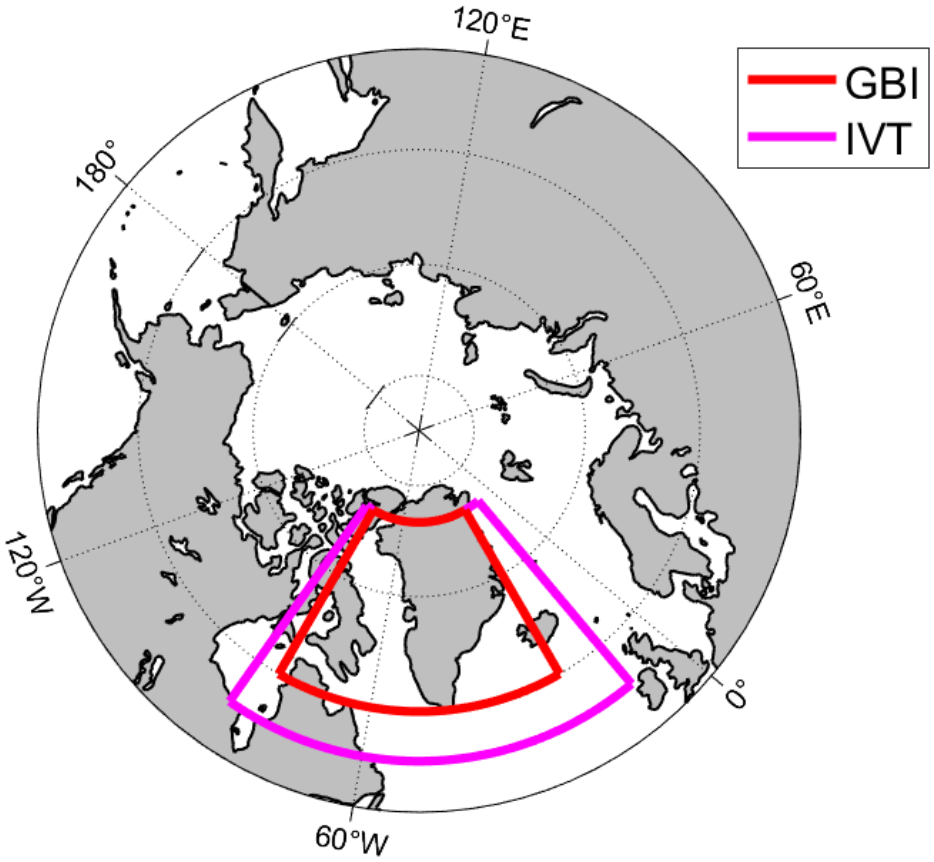


**Figure 3:** Spatial domains averaged to calculate the Greenland Blocking Index (GBI) index (red box region) and integrated vapor transport (IVT) (magenta boxed region), for both the ERA-Interim reanalysis product (1980-2019), and the 4 historical Climate Model Intercomparison Project 6 (CMIP6) model runs (1850-2015). The four CMIP6 historical model runs chosen included; the National Center for Atmospheric Research (NCAR), the Canadian Centre for Climate Modelling and Analysis (CCCma), the Max-Planck Institute of Meteorology (MPI), and the National Air and Space – Goddard Institute for Space Studies (NASA-GISS).

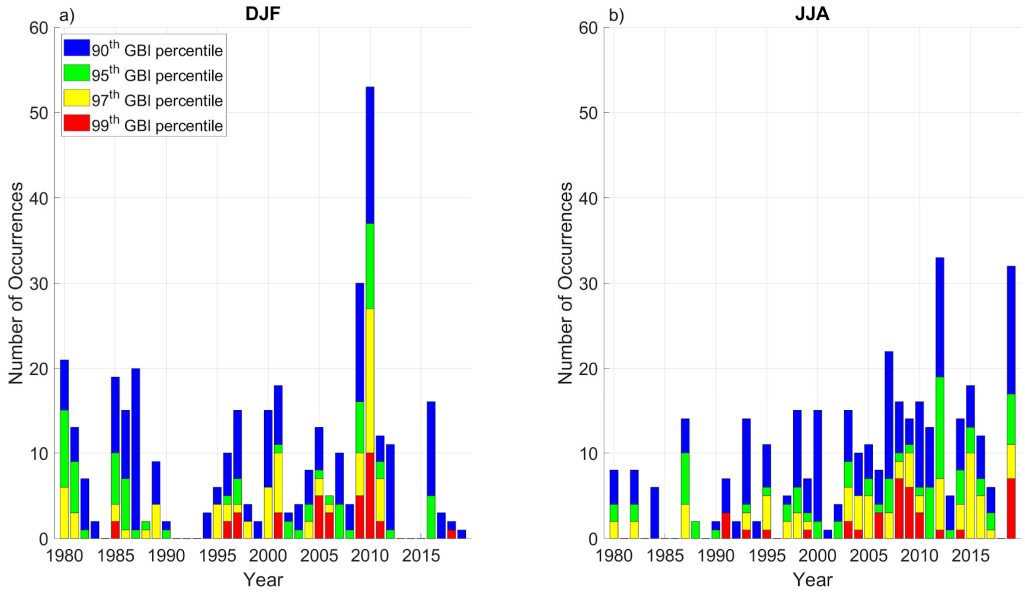


**Figure 4:** Frequency of extreme Greenland Blocking Index (GBI) days per year in the ERA-Interim reanalysis product (1980-2019) in (a) DJF and (b) JJA, at the 90th, 95th, 97th, and 99th percentiles for each season (Barrett et al. 2020).

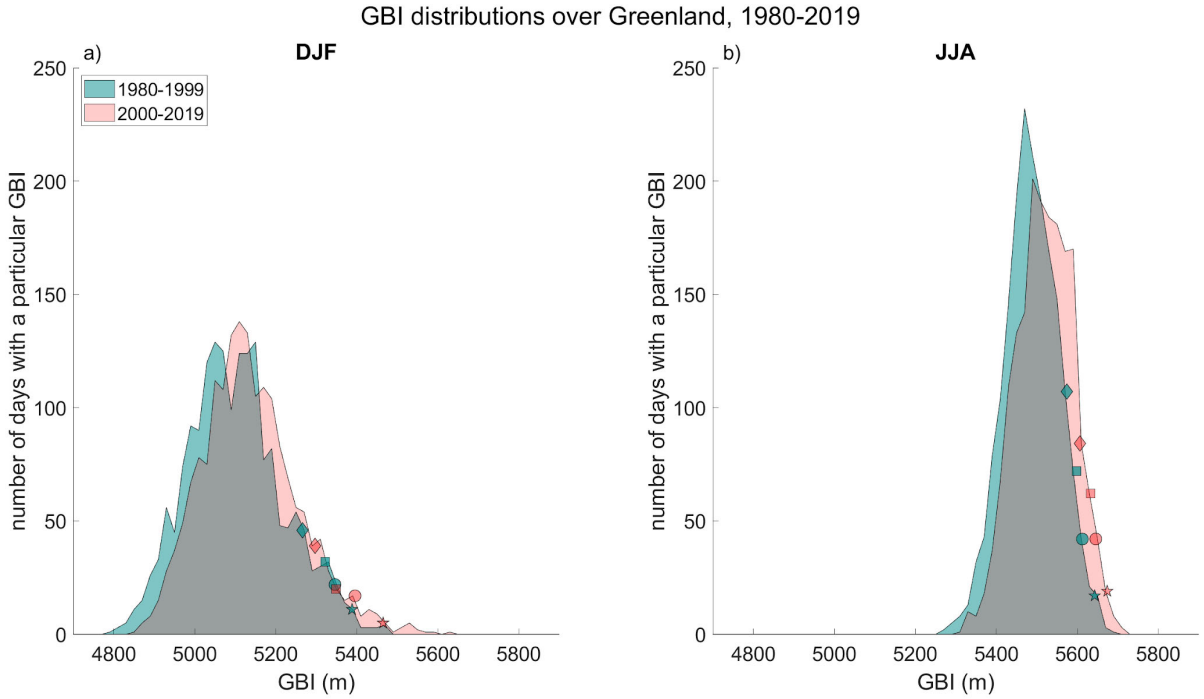


**Figure 5.** Distributions of the NOAA GBI index for 1980-1999 (teal distribution) and 2000-2019 (pink distribution) for (a) DJF and (b) JJA in the ERA-Interim reanalysis data. Diamond, square, circle, and star symbols in each plot indicate the 90th, 95th, 97th, and 99th percentile values, respectively. Figure from Barrett et al. 2020.

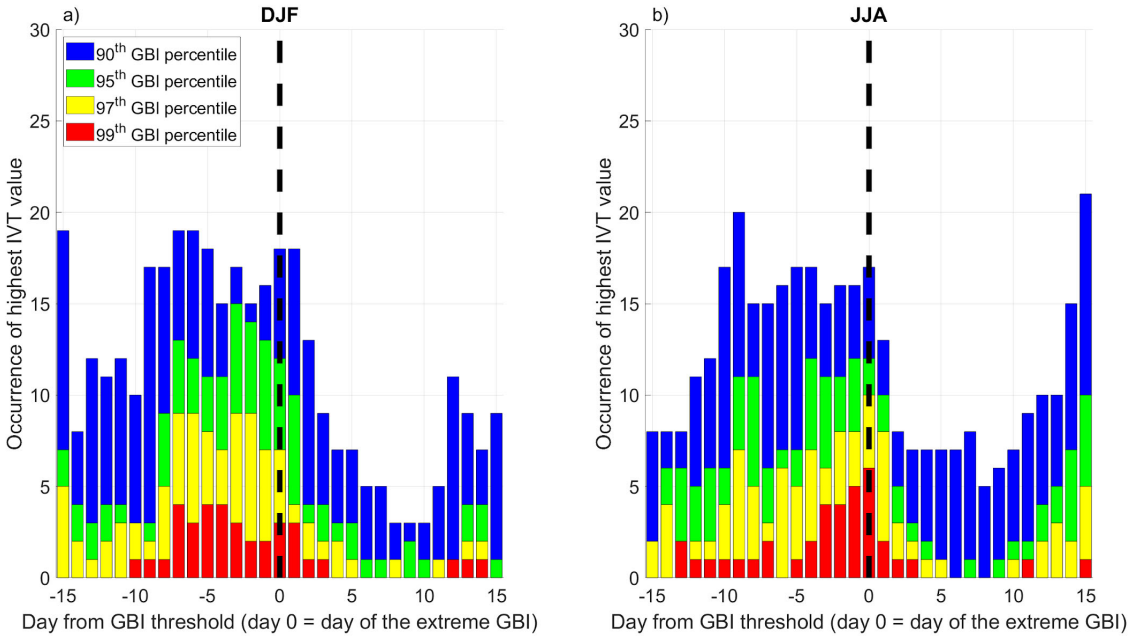


**Figure 6:** Frequency of above-average moisture transport for 15 days before to 15 days after an extreme blocking event in (a) DJF and (b) JJA in the ERA-Interim reanalysis product. Black dashed line indicates the day of extreme blocking, and colors indicate extremity of the blocking event (from 90th to 99th percentile). Figure from Barrett et al. 2020.

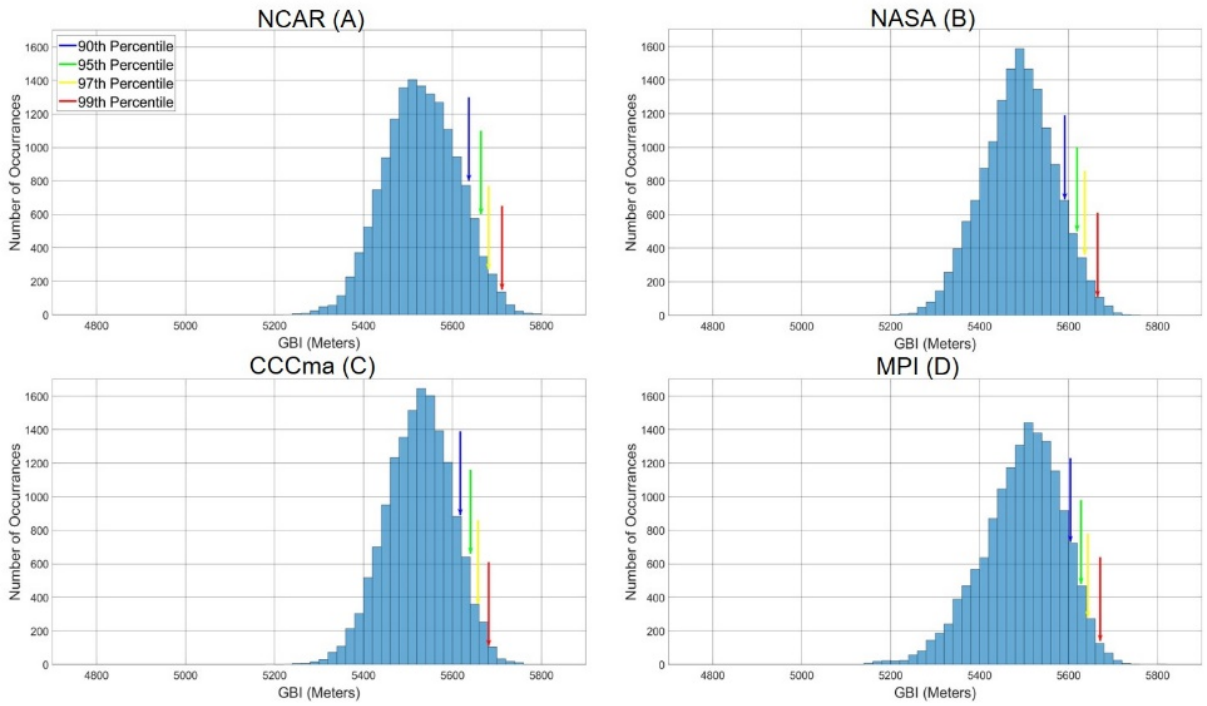


**Figure 7:** Distributions of extreme blocking during summer months (JJA), A) the National Center for Atmospheric Research (NCAR) model, B) the National Air and Space – Goddard Institute for Space Studies (NASA-GISS), C) the Canadian Centre for Climate Modelling and Analysis (CCCma) model, and D) the Max-Planck Institute of Meteorology (MPI). Each historical model run spanned from 1850-2015. For each distribution, both number of occurrences of blocking identified by the Greenland Blocking Index (GBI) in addition to the 90$^{th}$, 95$^{th}$, 97$^{th}$, and 99$^{th}$ percentile GBI values are indicated.

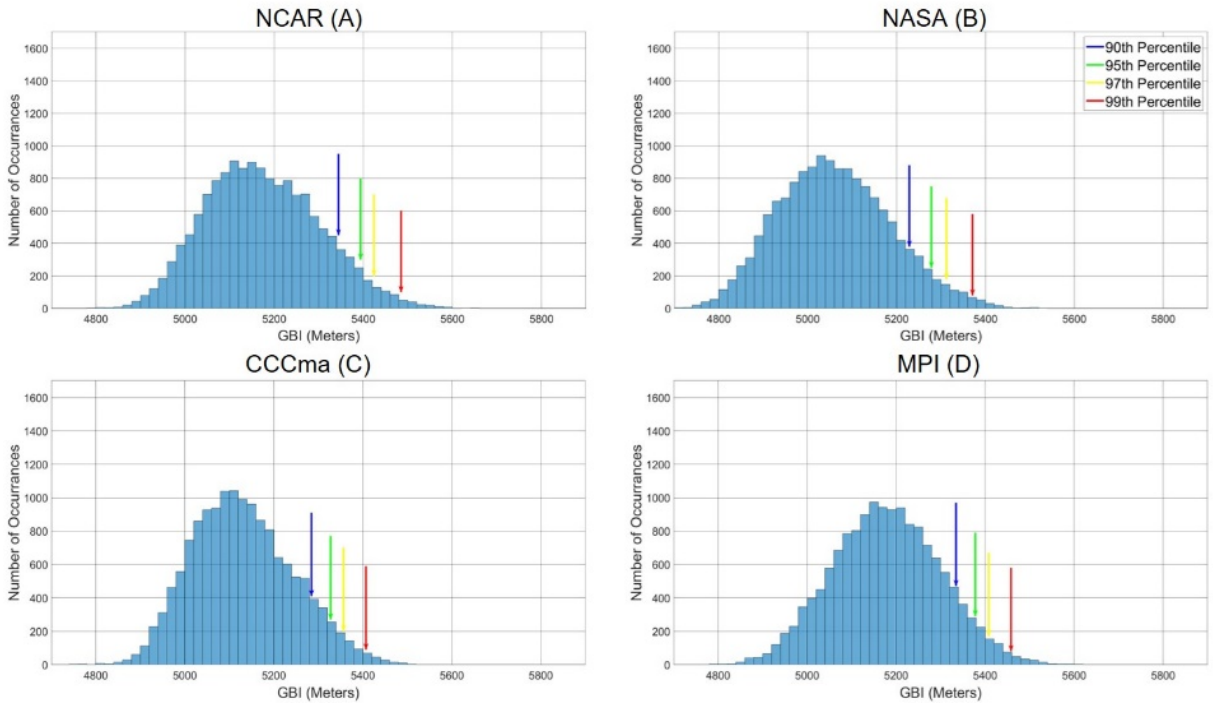


**Figure 8.** As in figure 7, for winder months (DJF).

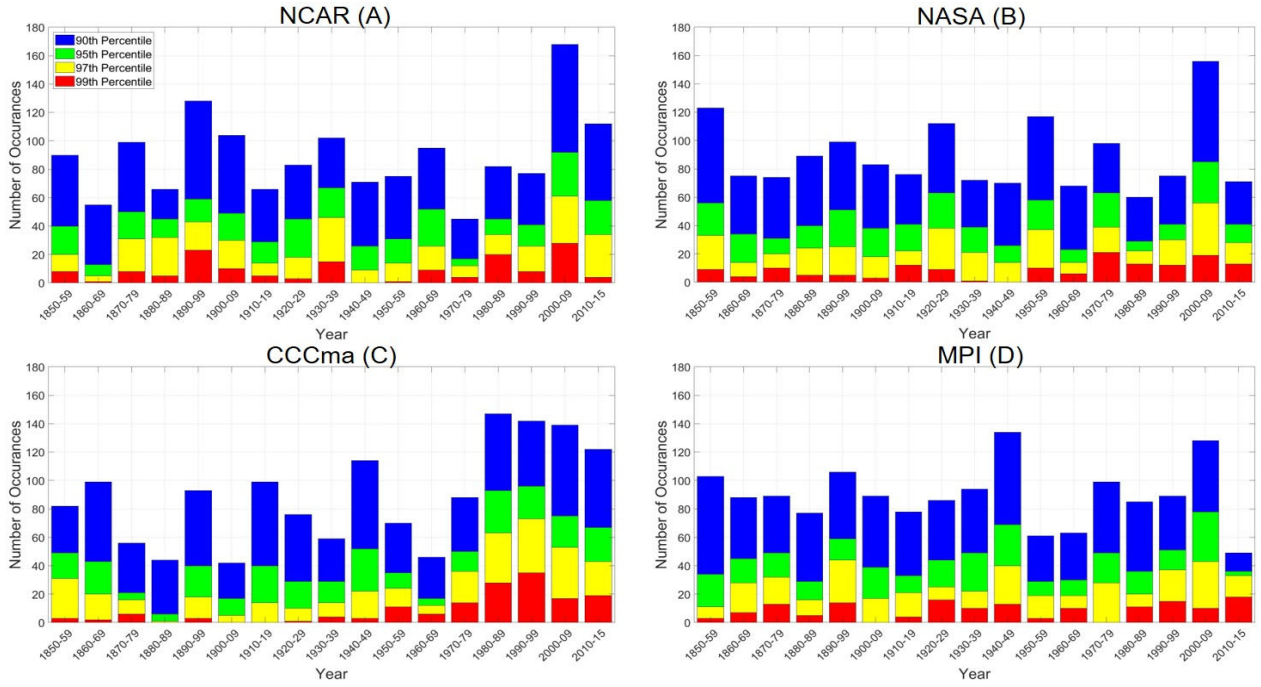


**Figure 9:** Frequency of extreme Greenland Blocking Index (GBI) days per year in, A) the National Center for Atmospheric Research (NCAR) model, B) the National Air and Space – Goddard Institute for Space Studies (NASA-GISS), C) the Canadian Centre for Climate Modelling and Analysis (CCCma) model, and D) the Max-Planck Institute of Meteorology (MPI), at the 90th, 95th, 97th, and 99th percentiles for June, July and August. CMIP6 models cover the time period from 1850-2015.

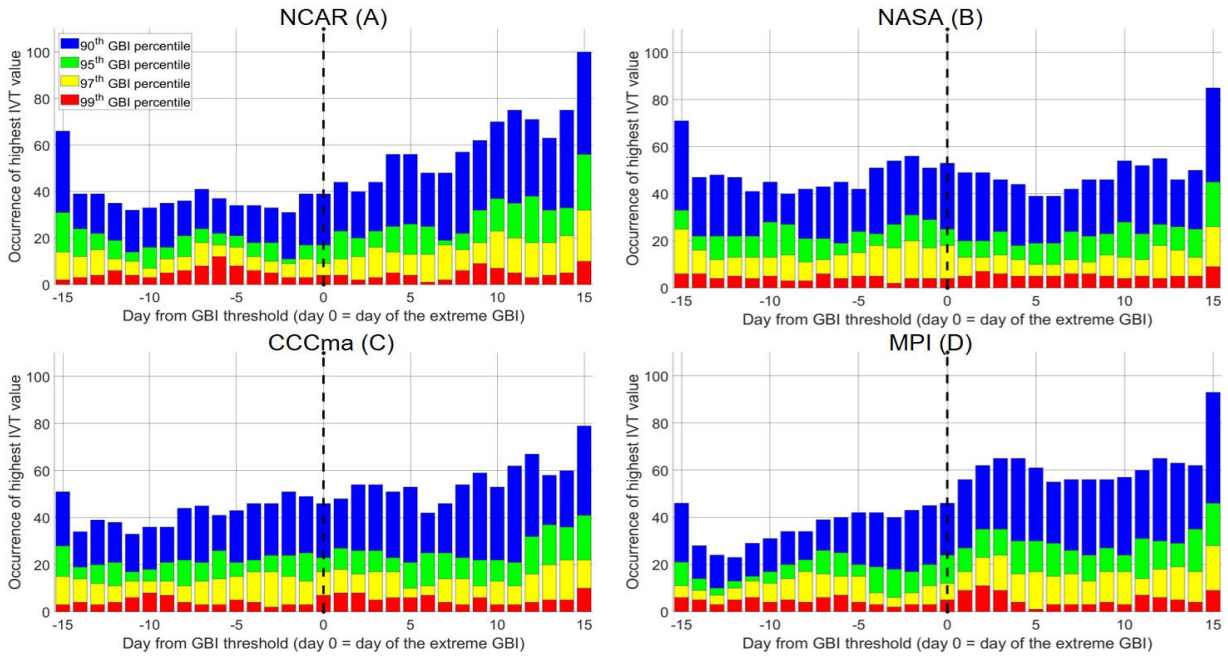


**Figure 10.** Frequency of above-average moisture transport for 15 days before to 15 days after an extreme blocking event in, A) the National Center for Atmospheric Research (NCAR) model, B) the National Air and Space – Goddard Institute for Space Studies (NASA-GISS), C) the Canadian Centre for Climate Modelling and Analysis (CCCma) model, and D) the Max-Planck Institute of Meteorology (MPI), at the 90th, 95th, 97th, and 99th percentiles for June, July and August. Black dashed line indicates the day of extreme blocking, and colors indicate extremity of the blocking event (from 90th to 99th percentile). CMIP6 models cover the time period from 1850-2015.

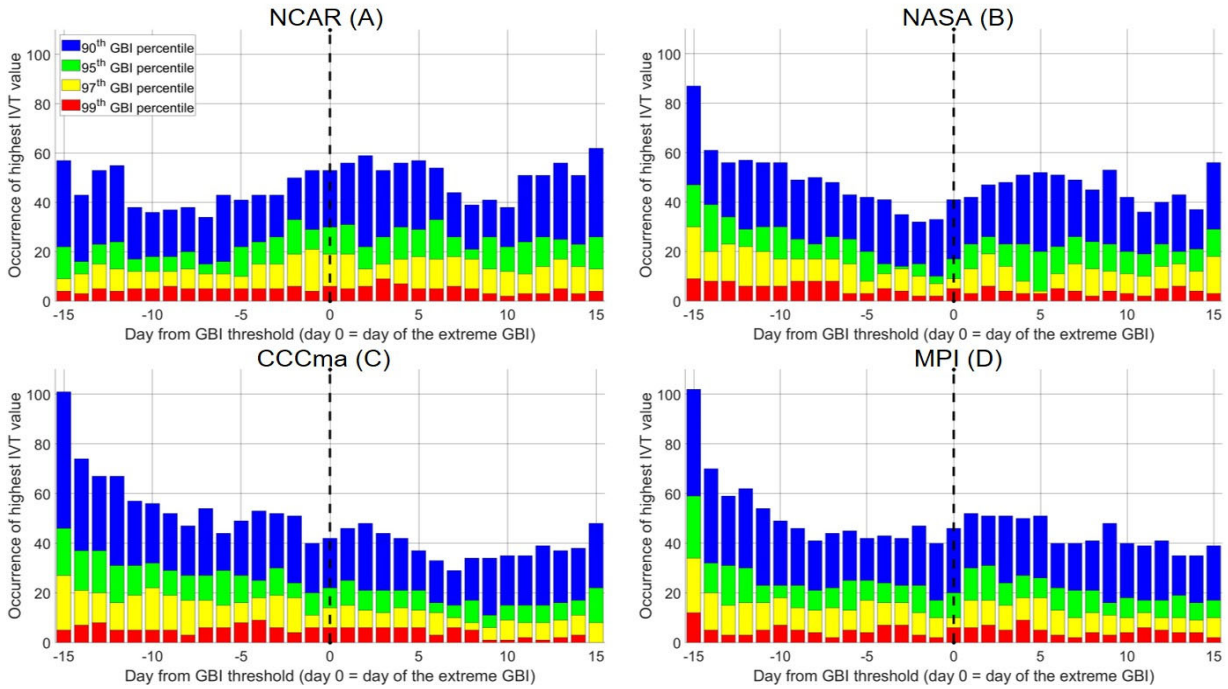


**Figure 11:** As in figure 10 for winter months (December, January and February).

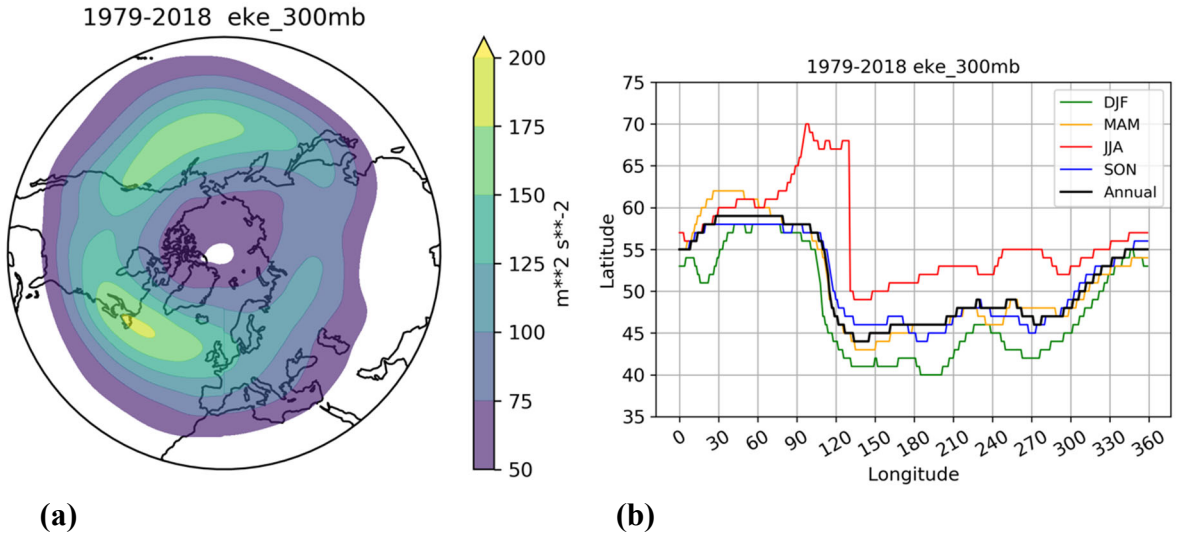


**(a)** **(b)**

**Figure 12**. (a) Annual mean bandpass filtered EKE for 1979-2018. (b) Latitude of annual mean (black line) and seasonal mean EKE (colored) at each longitude. Data were spatially smoothed with a Gaussian filter. Figure from Wachowicz et al. 2020.

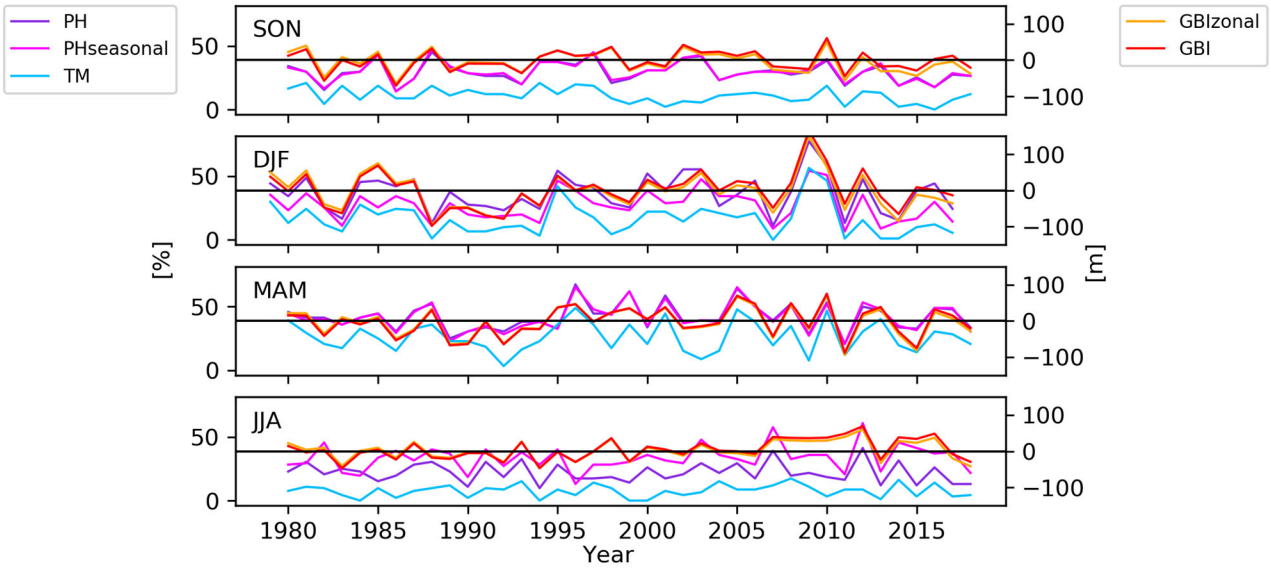


**Figure 13.** Time series of seasonal frequency of blocking (%) for the TM (blue), and traditional PH (purple), and modified PH (magenta) indices calculated as the total number of days per season with blocking criteria met (on the left y-axis). The monthly GBI anomalies (in meters) for the raw GBI (red) and GBI-Z (orange) are associated with the rightmost y-axis. Note: the horizontal line corresponds to where y = 0 [m] for the GBI anomaly calculations, associated with the rightmost y-axis. Figure from Wachowicz et al. 2020.

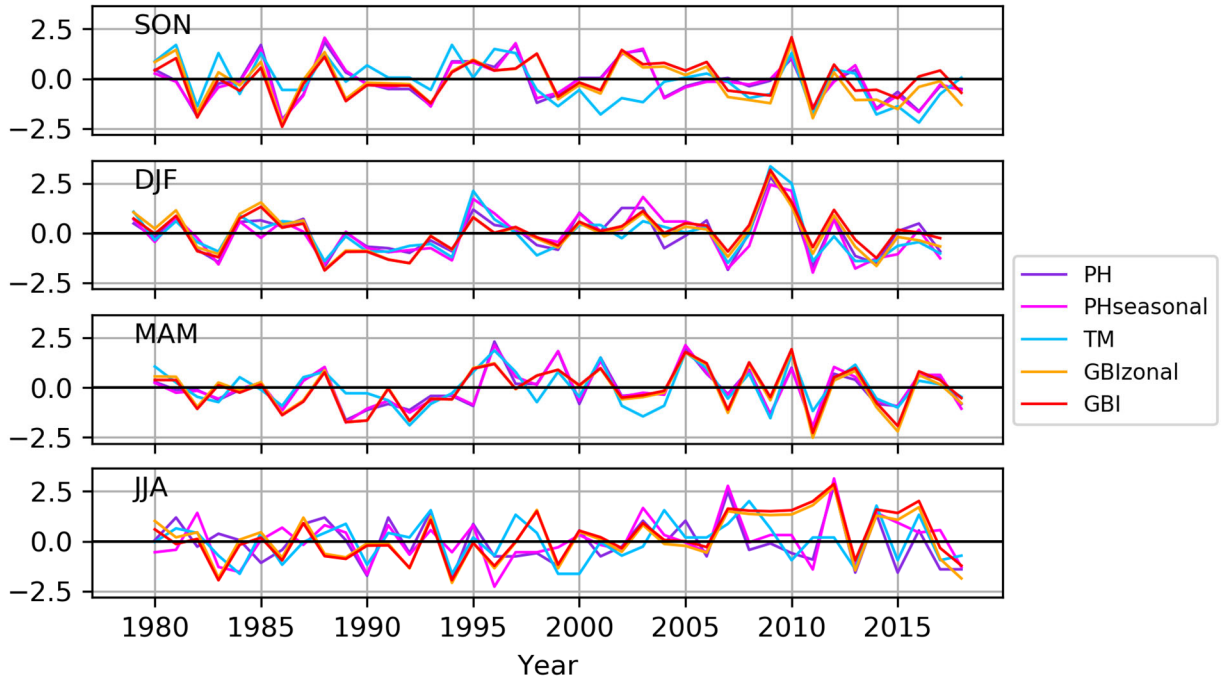


**Figure 14.** Standardized seasonal blocking frequency, with respect to the 1981-2010 (1980-2009 for DJF) reference period. Year refers to the year in which December occurred. Figure from Wachowicz et al. 2020.

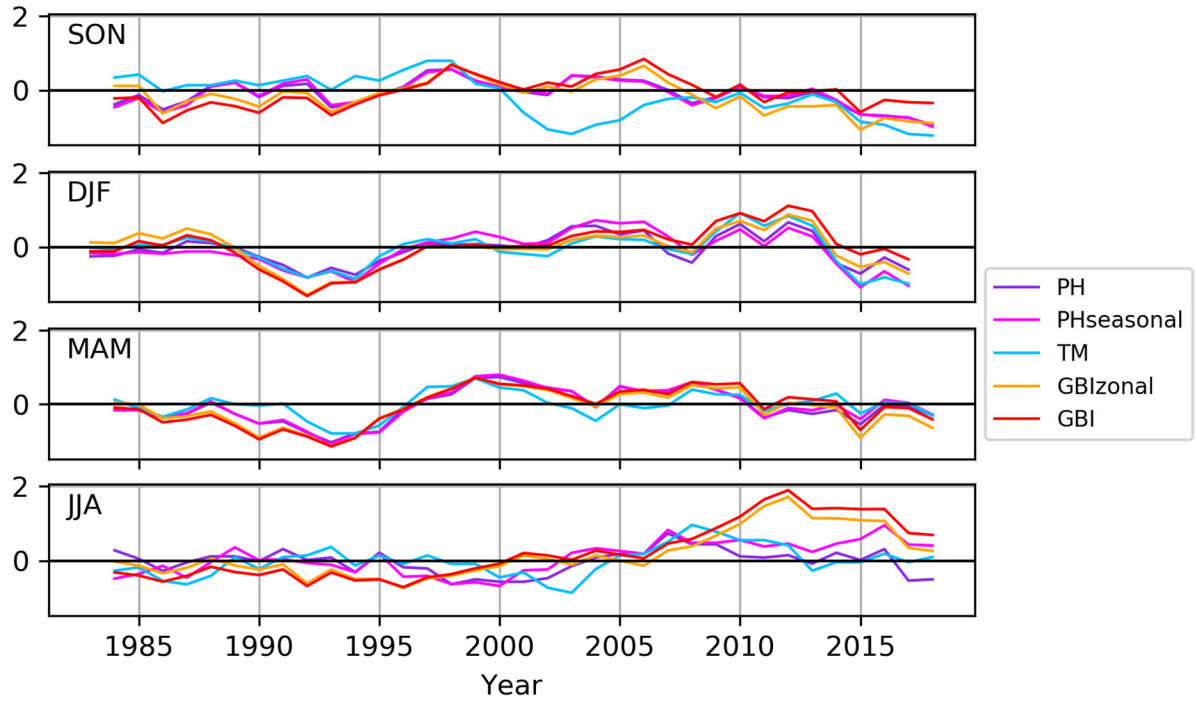


**Figure 15.** Time series of 5-year running mean of standardized seasonal blocking frequency anomalies. Year refers to the year in which December occurred. Figure from Wachowicz et al. 2020.

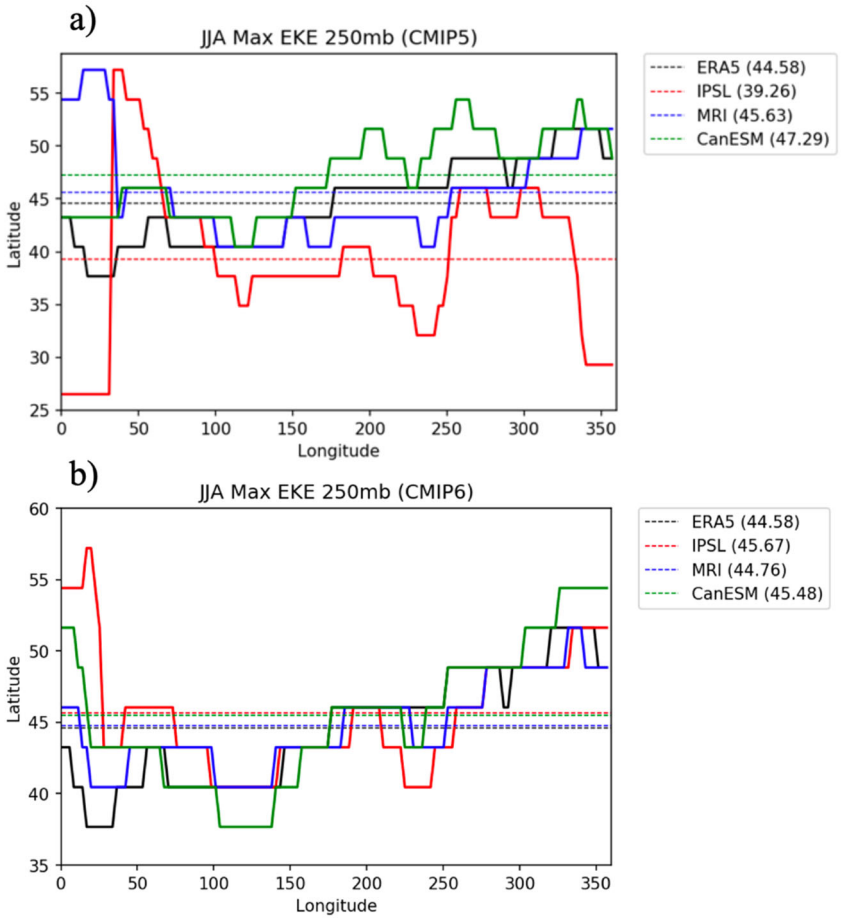


**Figure 16.** Total number of longitude cells per JJA season which experience blocking conditions at 54.5$^{o}$ latitude for (a) CMIP5 models and (b) CMIP6 models.

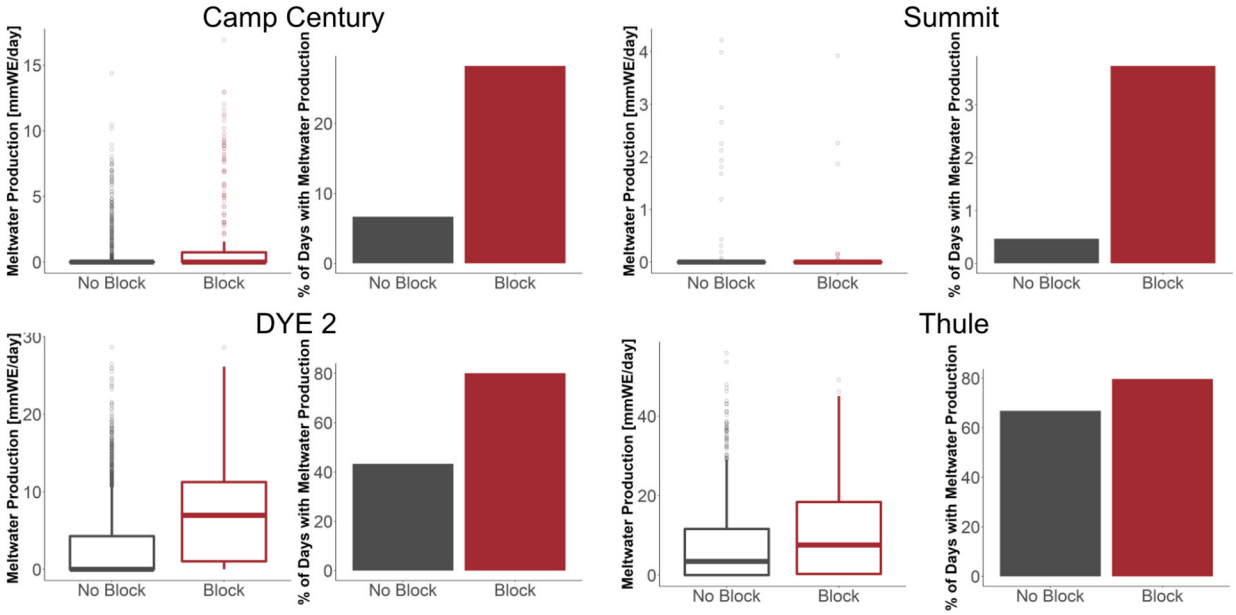


**Figure 17:** Number of days (%) with meltwater production (bar chart) and amount of meltwater production (boxplot) for blocked and unblocked conditions at Camp Century, Summit, DYE-2, and Thule.

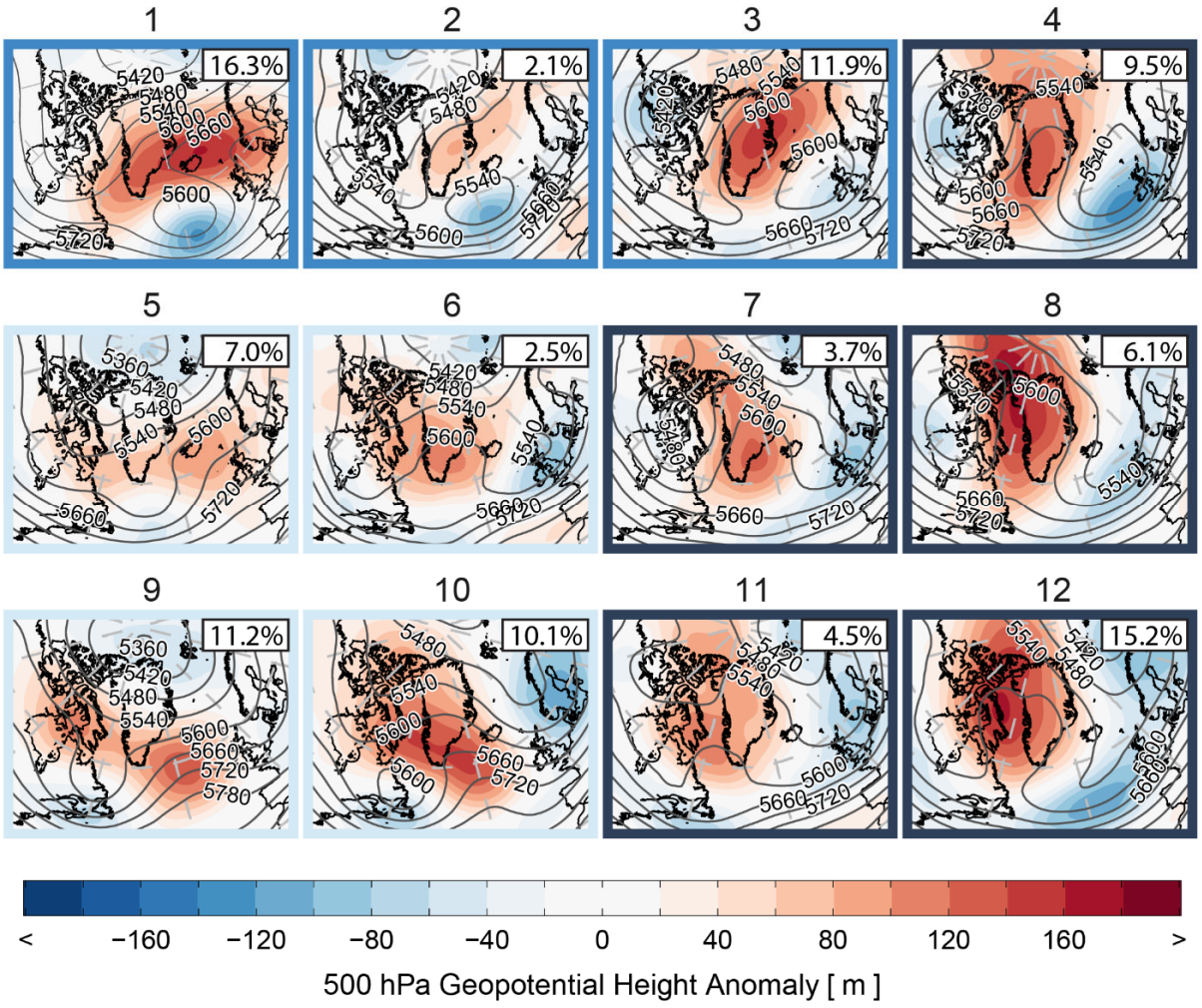


**Figure 18:** Composite anomalies (shading) and composite means (contours: 60m interval) of 500 hPa geopotential height for all JJA blocking episode days identified separately by PH03 and GBI and composited by SOM BMU. The frequency of each node with respect to all blocking episode days displayed in the upper right corner. Map outlines indicate subjective groupings: Omega (dark blue), CWB (medium blue), or SR (light blue). Figure from Preece et al. 2022.

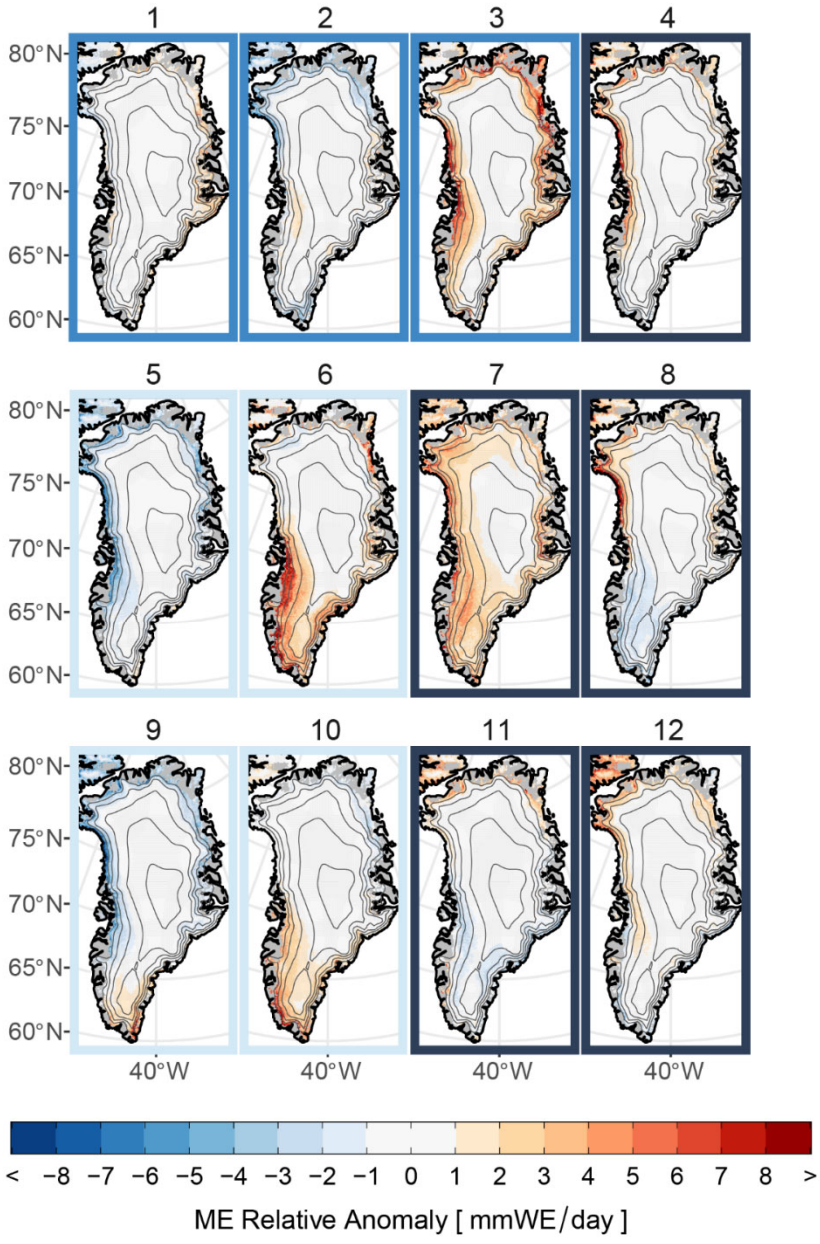


**Figure 19:** The composite anomaly of ME for each SOM node less the composite anomaly for all blocking episode days. Contours denote MAR elevation data; contour interval of 500m from 1000–3000m. Figure from Preece et al. 2022.

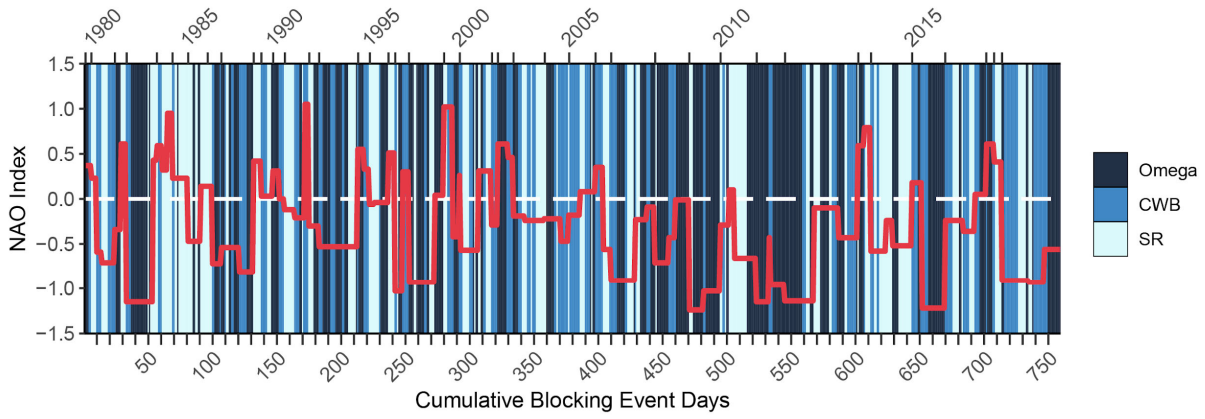


**Figure 20:** Stripe diagram of the subjective group assignments for all cumulative JJA blocking episode days identified separately by PH03 and GBI. Stripe color denotes group assignments consistent with color-coding in Figure 18. Top axis denotes the first blocking episode day of each year. Red line shows monthly NAO index value (y-axis) for each blocking episode day. Note that the spacing of the tick marks along the top axis is proportional to the number of blocking episode days in a period—e.g., blocking frequency was greater in 2010–2015 than in 1995–2000.

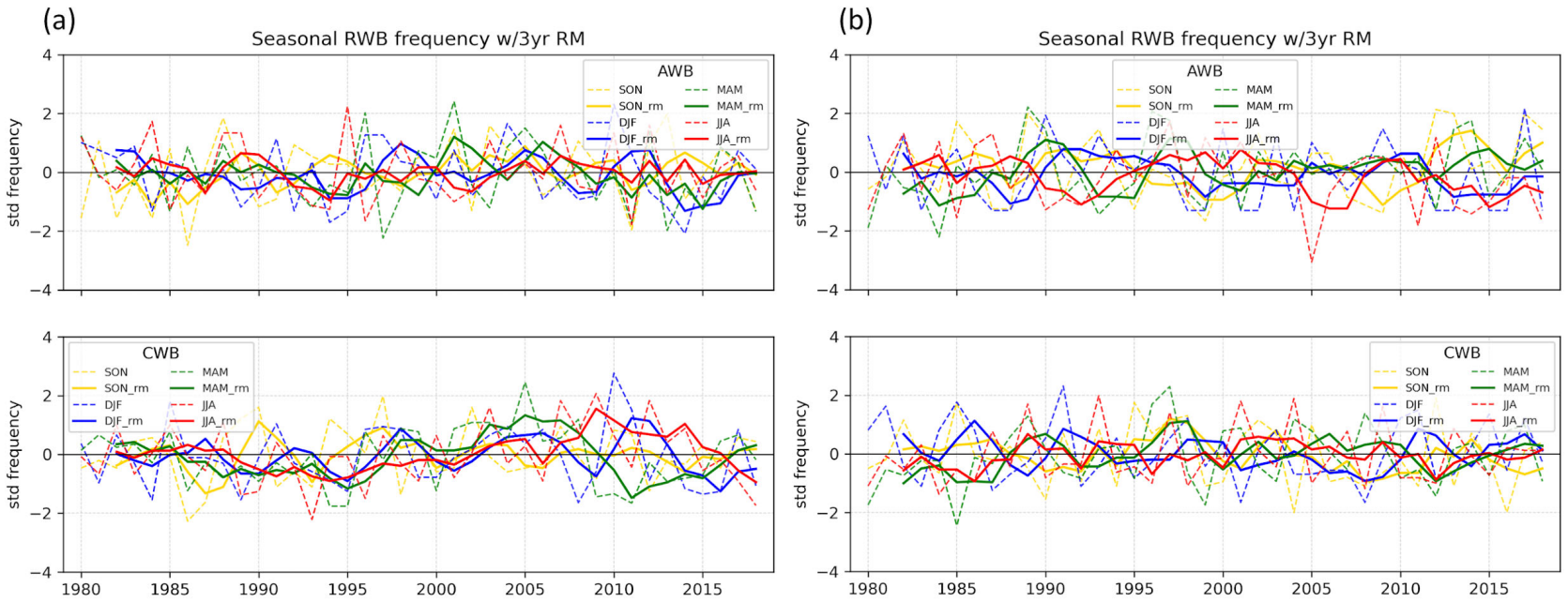


**Figure 21:** Standardized counts of number of days per season with wave breaking criteria for (a) North Atlantic and (b) North Pacific. Included are all events lasting 2 or more days. A 3-year running mean is applied (bolded line). Frequencies are standardized with respect to the 1981-2010 mean. Figure from Wachowicz et al. (in prep, Clim. Dyn.).

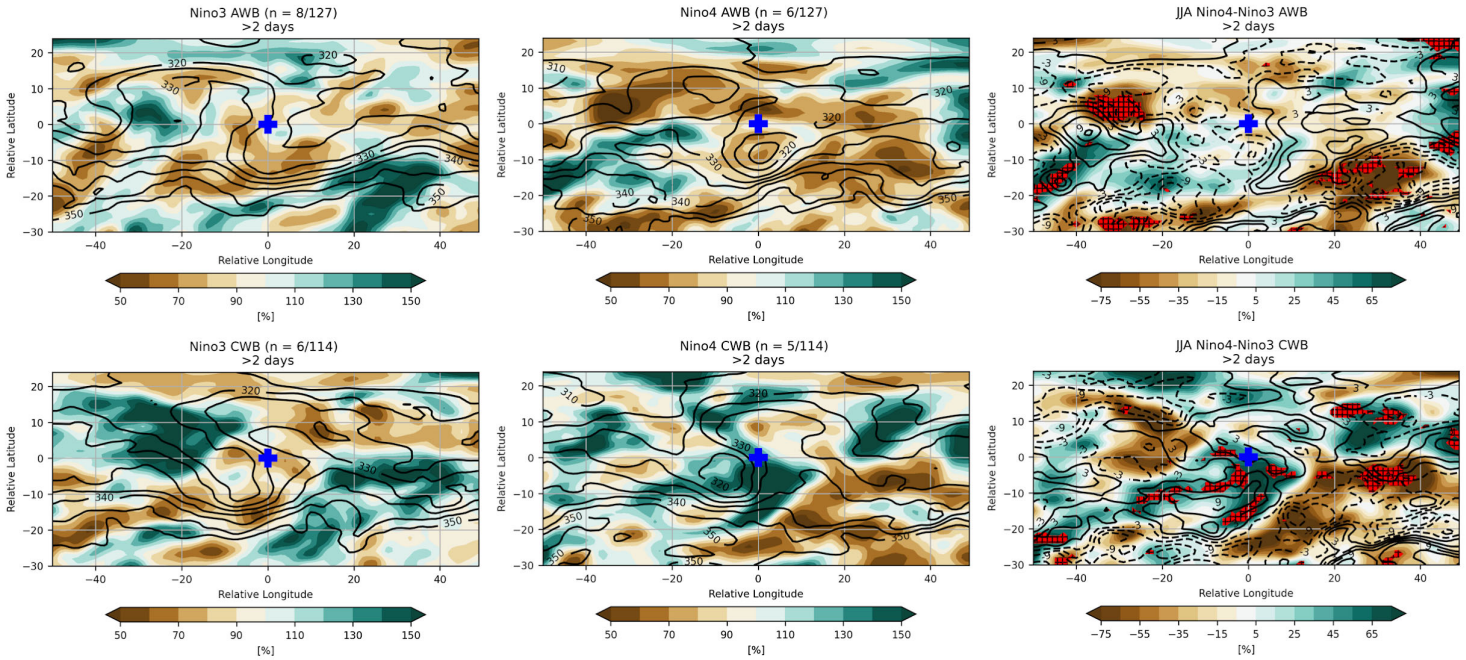


**Figure 22:** North Atlantic %IVT relative to all RWB events lasting 3 or more days in JJA seasons of positive SST anomalies. Significance at 90% using Mann Whitney U test (red shading). Figure from Wachowicz et al. (in prep, Clim. Dyn.).

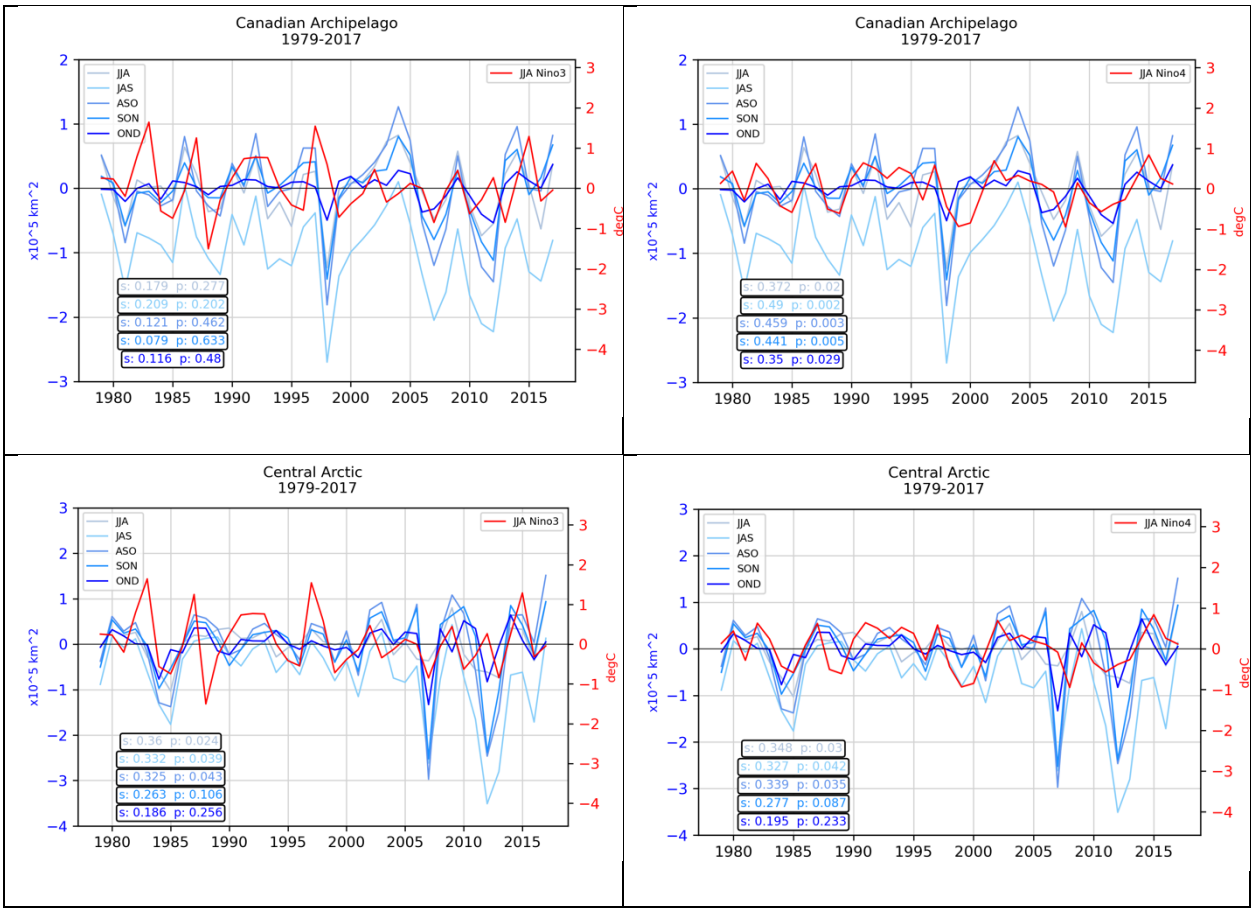


**Figure 23:** Detrended seasonal sea ice area from Walsh et al. (2019) and 3-month average detrended Niño3 (left)/ Niño4 (right) time series for the Canadian Archipelago (top) and Central Arctic (bottom). Pearson correlation (s) for JJA SSTs and 3-month average sea ice area and p-value (p) shown. Figure from Wachowicz et al. (in prep, J. Geophys. Res. Atm.).

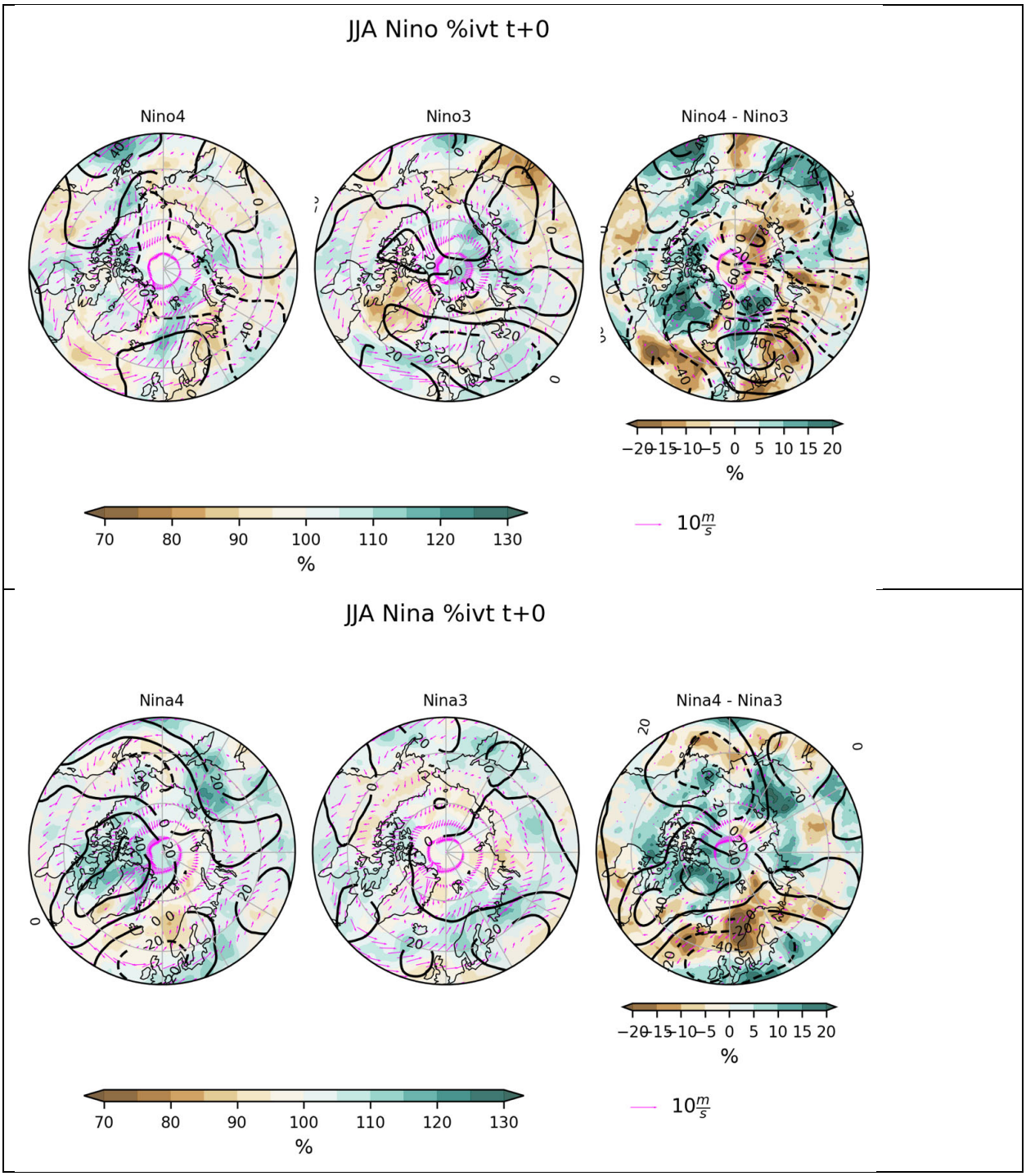


**Figure 24:** ERA5 composites of the JJA 500 hPa height anomalies (black contours), integrated vapor transport (IVT) expressed as a % of the seasonal mean (filled), and 850 hPa seasonal mean wind (magenta) for Nino (top) and Nina (bottom) seasons. Figure from Wachowicz et al. (in prep. J. Geophys. Res. Atm.)

# Literature cited:


Blackmon, M. L., and G. H. White, 1982: Zonal wavenumber characteristics of Northern Hemisphere transient eddies. *Journal of the Atmospheric Sciences*, 39, 1985-1998, doi:10.1175/1520-0469(1982)039<1985:ZWCONH>2.0.CO;2.

Bowley, K. A., J. R. Gyakum, and E. H. Atallah, 2019: A New Perspective toward Cataloging Northern Hemisphere Rossby Wave Breaking on the Dynamic Tropopause. Monthly Weather Review, 147, 409-431, doi:10.1175/MWR-D-18-0131.1.

Brodzik, M. J., Billingsley, B., Haran, T., Raup, B., & Savoie, M. H., 2012: EASE-Grid 2.0: Incremental but significant improvements for earth-gridded data sets. ISPRS International Journal of Geo-Information, 1(1), 32–45. https://doi.org/10.3390/ijgi1010032

Brodzik, M. J., Billingsley, B., Haran, T., Raup, B., & Savoie, M. H., 2014: Correction: Brodzik, M.J., et al. EASE-Grid 2.0: Incremental but significant improvements for earth-gridded data sets. ISPRS International Journal of Geo-Information 2012, 1, 32–45. ISPRS International Journal of Geo-Information, 3(3), 1154–1156. https://doi.org/10.3390/ijgi3031154

DuVivier, A. K., M. M. Holland, J. E. Kay, S. Tilmes, A. Gettelman, and D. A. Bailey, 2020: Arctic and Antarctic Sea Ice Mean State in the Community Earth System Model Version 2 and the Influence of Atmospheric Chemistry. Journal of geophysical research. Oceans, 125, n/a, doi:10.1029/2019JC015934.

Fettweis, X., Gallée, H., Lefebre, F., & van Ypersele, J.-P., 2005: Greenland surface mass balance simulated by a regional climate model and comparison with satellite-derived data in 1990–1991. Climate Dynamics, 24(6), 623–640. https://doi.org/10.1007/s00382-005-0010-y

Fettweis, X., Box, J., Agosta, C., Amory, C., Kittel, C., Lang, C., et al., 2017: Reconstructions of the 1900–2015 Greenland ice sheet surface mass balance using the regional climate MAR model. Cryosphere, 11. https://doi.org/10.5194/tc-11-1015-2017

Freund, M. B., B. J. Henley, D. J. Karoly, H. V. McGregor, N. J. Abram, and D. Dommenget, 2019: Higher frequency of Central Pacific El Niño events in recent decades relative to past centuries. Nature Geoscience, 12, 450-455, doi:10.1038/s41561-019-0353-3.

Gettelman, A., C. Hannay, J.T. Bacmeister, R.B. Neale, A.G. Pendergrass, G. Danabasoglu, J.F. Lamarque, J.T. Fasullo, D.A. Bailey, D.M. Lawrence, and M.J. Mills, 2019: High climate sensitivity in the Community Earth System Model version 2 (CESM2). Geophysical Research Letters, 46(14), 8329-8337.

Hanna, E., T. E. Cropper, R. J. Hall, and J. Cappelen, 2016: Greenland Blocking Index 1851–2015: a regional climate change signal. *International Journal of Climatology,* 36, 4847-4861, doi:10.1002/joc.4673.

Henderson, G.R., Barrett, B.S., Wachowicz, L.J., Mattingly, K.S., Preece, J.R. and Mote, T.L., 2021: Local and Remote Atmospheric Circulation Drivers of Arctic Change: A Review. Front. Earth Sci. 9:709896. doi: 10.3389/feart.2021.709896

Henderson, G. R., B. S. Barrett, and K. L. South, 2017: Eurasian October snow water equivalent: using self-organizing maps to characterize variability and identify relationships to the MJO. *International Journal of Climatology*, 37, 596-606. doi:10.1002/joc.4725.

Hersbach, H., Bell, B., Berrisford, P., Biavati, G., Horányi, A., Muñoz-Sabater, J., … Thépaut, J.-N., 2018: ERA5 hourly data on pressure levels from 1979 to present. Copernicus

Climate Change Service (C3S) Climate Data Store (CDS). Accessed on 18-MAR-2021. https://doi.org/10.24381/cds.bd0915c6

Hewitson, B. C., & Crane, R. G., 2002: Self-organizing maps: applications to synoptic climatology. Climate Research, 22(1), 13–26. https://doi.org/10.3354/cr022013

Hu, C., S. Yang, Q. Wu, Z. Li, J. Chen, K. Deng, T. Zhang, and C. Zhang, 2016: Shifting El Niño inhibits summer Arctic warming and Arctic sea-ice melting over the Canada Basin. Nature Communications, 7, 1-9, doi:10.1038/ncomms11721.

Kay, J. E., C. Deser, A. Phillips, A. Mai, C. Hannay, G. Strand, J. M. Arblaster, S. C. Bates, G. Danabasoglu, J. Edwards, M. Holland, P. Kushner, J.-F. Lamarque, D. Lawrence, K. Lindsay, A. Middleton, E. Munoz, R. Neale, K. Oleson, L. Polvani, and M. Vertenstein, 2015: The Community Earth System Model (CESM) Large Ensemble Project: A Community Resource for Studying Climate Change in the Presence of Internal Climate Variability. Bulletin of the American Meteorological Society, 96, 1333.

Kohonen, T., 1990: The self-organizing map. Proceedings of the IEEE, 78(9), 1464–1480. https://doi.org/10.1109/5.58325

Lefebre, F., Fettweis, X., Gallée, H., Van Ypersele, J.-P., Marbaix, P., Greuell, W., & Calanca, P., 2005: Evaluation of a high-resolution regional climate simulation over Greenland. Climate Dynamics, 25(1), 99–116. https://doi.org/10.1007/s00382-005-0005-8

Liu, C., and E. A. Barnes, 2015: Extreme moisture transport into the Arctic linked to Rossby wave breaking. *Journal of Geophysical Research: Atmospheres*, 120(9), 3774–3788.

Masato, G., B. J. Hoskins, and T. J. Woollings, 2012: Wave-breaking characteristics of midlatitude blocking. *Quarterly Journal of the Royal Meteorological Society,* 138, 1285-1296, doi:10.1002/qj.990.

Masato, G., B. J. Hoskins, and T. Woollings, 2013: Wave-Breaking Characteristics of Northern Hemisphere Winter Blocking: A Two-Dimensional Approach. *Journal of Climate,* 26, 4535-4549, doi:10.1175/JCLI-D-12-00240.1.

Mattingly, K. S., C. A. Ramseyer, J. J. Rosen, T. L. Mote, R. Mythyala, 2016: Increasing water vapor transport to the Greenland Ice Sheet revealed using self-organizing maps, Geophys. Res. Lett., 43, 9250-9258, doi: 10.1002/2016GL070424.

Mattingly, K. S., T. L. Mote, and X. Fettweis, 2018: Atmospheric river impacts on Greenland Ice Sheet surface mass balance. *Journal of Geophysical Research: Atmospheres*, 123(16), 8538–8560.

McIlhattan, E. A., J. E. Kay, and T. S. L'Ecuyer, 2020: Arctic clouds and precipitation in the Community Earth System Model version 2. Journal of Geophysical Research: Atmospheres, 125, e2020JD032521.

Miljković, D., 2017: Brief review of self-organizing maps. In 2017 40th International Convention on Information and Communication Technology, Electronics and Microelectronics (MIPRO) (pp. 1061–1066). https://doi.org/10.23919/MIPRO.2017.7973581

Noël, B., Berg, W. J. van de, Lhermitte, S., & van den Broeke, M. R., 2019: Rapid ablation zone expansion amplifies north Greenland mass loss. Science Advances, 5(9), eaaw0123. https://doi.org/10.1126/sciadv.aaw0123

Pelly, J. L., and B. J. Hoskins, 2003: A new perspective on blocking. *Journal of the Atmospheric Sciences*, 60 (5), 743–755.

Reusch, D. B., Alley, R. B., & Hewitson, B. C., 2005: Relative performance of self-organizing maps and principal component analysis in pattern extraction from synthetic

climatological data. Polar Geography, 29(3), 188–212. https://doi.org/10.1080/789610199
Sheridan, S. C., & Lee, C. C., 2011: The self-organizing map in synoptic climatological research. Progress in Physical Geography: Earth and Environment, 35(1), 109–119. https://doi.org/10.1177/0309133310397582
Slater, T., Hogg, A. E., & Mottram, R., 2020: Ice-sheet losses track high-end sea-level rise projections. Nature Climate Change, 10(10), 879–881. https://doi.org/10.1038/s41558-020-0893-y
Tedesco, M., & Fettweis, X., 2020: Unprecedented atmospheric conditions (1948–2019) drive the 2019 exceptional melting season over the Greenland ice sheet. Cryosphere, 14, 1209–1223. https://doi.org/10.5194/tc-14-1209-2020
Tibaldi, S., and Molteni, F., 1990: On the operational predictability of blocking. *Tellus A: Dynamic Meteorology and Oceanography*, 42, 343–365.
Wachowicz*, L.J., Preece*, J.R., Mote, T.L., 2021: Barrett, B.S., Henderson, G.R. Historical trends of seasonal Greenland blocking under different blocking metrics. *Int J Climatol*; 41 (Suppl. 1): E3263– E3278. https://doi.org/10.1002/joc.6923
Walsh, J. E., W. L. Chapman, F. Fetterer, and J. S. Stewart. 2019. Gridded Monthly Sea Ice Extent and Concentration, 1850 Onward, Version 2. [Indicate subset used]. Boulder, Colorado USA. NSIDC: National Snow and Ice Data Center. doi:https://doi.org/10.7265/jj4s-tq79. [10 October 2020].
Yang, W. and G. Magnusdottir, 2018: Year-to-year Variability in Arctic Minimum Sea Ice Extent and its Preconditions in Observations and the CESM Large Ensemble Simulations. Scientific reports, 8, 9070-7, doi:10.1038/s41598-018-27149-y.

# Appendices:

## A. List of Scientific/Technical Publications

### 1. Publications in peer-reviewed journals:

**Indicates student author*


Barrett, B.S., G.R. Henderson. E. McDonnell*, M. Henry*, N. Cartwright*, T. Mote, 2020: Extreme Greenland blocking and high-latitude moisture transport. *Atmospheric Research Letters*. 2020; 21:e1002. https://doi.org/10.1002/asl.1002

Henderson, G.R., Barrett, B.S., Wachowicz*, L.J., Mattingly, K.S., Preece*, J.R. and Mote, T.L., 2021: Local and Remote Atmospheric Circulation Drivers of Arctic Change: A Review. Front. Earth Sci. 9:709896. doi: 10.3389/feart.2021.709896

Mikulak, H., 2020: Influence of low-frequency atmospheric teleconnections on Arctic blocking patterns. M.S. Thesis, University of Georgia, Athens GA, 99pp.

Preece, J. R.*, Wachowicz, L. J.*, Mote, T. L., Tedesco, M., Fettweis, X., 2022: Summer Greenland Blocking Diversity and its Impact on the Surface Mass Balance of the Greenland Ice Sheet. Journal of Geophysical Research: Atmospheres. 127, e2021JD035489. https://doi.org/10.1029/2021JD035489

Wachowicz*, L.J., Preece*, J.R., Mote, T.L., 2021: Barrett, B.S., Henderson, G.R. Historical trends of seasonal Greenland blocking under different blocking metrics. *Int J Climatol*; 41 (Suppl. 1): E3263– E3278. https://doi.org/10.1002/joc.6923

Wachowicz, L.* and T. Mote: Quantifying Tropical Contributions from El Niño Diversity to Arctic Moisture Transport from Rossby Wave Breaking. (Climate Dynamics, *in preparation*).

Wachowicz, L.* and T. Mote: Connecting ENSO and Arctic Sea Ice Spatial and Seasonal Variability through Atmospheric Linkages. (J. Geophysical Research: Atmospheres, *in preparation*).


### 2. Conference Presentations:

***Year 1 presentations:***


Henderson, G. R., B. S. Barrett, T. Mote, E. McDonnell, M. Henry, 2018: Impacts on high-latitude DoD infrastructure and operations from melt events driven by large-scale low-frequency atmospheric circulations. Presented at the SERDP Symposium, Washington DC, November 2018.

Henderson, G.R., B.S. Barrett, E. McDonnell, M. Henry, 2019: Quantifying the impact of atmospheric blocking on the mean state of the North Atlantic Sector of the Arctic.

Presented at the American Meteorological Society Annual meeting, Phoenix, AZ, 6-10th January 2019.

Mikulak, H., T. Mote, G. Henderson, and B. Barrett, 2019: Seasonal and Regional Variations in Arctic Blocking Patterns. Presented at American Association of Geographers Annual Meeting, Washington, DC.

Mikulak, H., T. Mote, G. Henderson, and B. Barrett, 2019: Influence of Low-Frequency Atmospheric Teleconnection Patterns on Arctic Blocking Patterns. Presented at 15th Conference on Polar Meteorology and Oceanography, American Meteorological Society, Boulder, CO.

Wachowicz, L. J., H. Mikulak, K. Mattingly, T. Mote, B. Barrett, and G. Henderson, 2019: Role of Extreme Anticyclone Blocking and Moisture Transport on Surface Mass Balance and Energy Budget of Greenland: A Case Study Approach. Presented at 15th Conference on Polar Meteorology and Oceanography, Boulder, CO.

Wachowicz, L. J., H. Mikulak, K. Mattingly, and T. Mote, 2019: Relationships between episodes of extreme atmospheric blocking, moisture transport, and surface mass balance of Greenland. Presented at American Association of Geographers Annual Meeting, Washington, DC.

***Year 2 presentations:***

Cartwright, N., G.R. Henderson, B.S. Barrett, 2020: Extreme Blocking in the North Atlantic Arctic in Future Climates. American Meteorological Society Annual meeting, Boston, MA, January 2020.

Henderson, G.R., B. S. Barrett, N. Cartwright, 2019: Impacts on high-latitude DoD infrastructure and operations from melt events driven by large-scale low-frequency atmospheric circulations. Presented at the SERDP Symposium, Washington DC, December 2019.

Henderson, G.R., B.S. Barrett, T. Mote, N. Cartwright, 2020: Quantifying the impact of atmospheric blocking on the mean state of the North Atlantic sector of the Arctic. American Meteorological Society Annual meeting, Boston, MA, January 2020.

Mote, T., L. Wachowicz, J. Preece, K. Mattingly, and T. Ballinger: Sources of anomalous air masses associated with melting of the Greenland Ice Sheet. Presented at *American Association of Geographers Annual Meeting*, April 2020, Denver, CO.

Wachowicz, L., J. Preece, T. Mote, G. Henderson, and B. Barrett: Understanding Arctic Blocking Representation in Climate Models under a Unique Framework. Presented at *American Geophysical Union Fall Meeting*, December 2019, San Francisco, CA.

***Year 3 presentations:***

Henderson, G.R., B.S. Barrett, T. Mote. Quantifying the impact of moisture transport during extreme blocking events in the North Atlantic as represented in the CMIP6 model suite. To be Presented at American Geophysical Union Fall Meeting, New Orleans, LA.

Preece, J. R.*, Wachowicz, L. J.*, Mote T. L., Tedesco M. Contrasting the Greenland Ice Sheet Surface Energy Balance Response Between Predominate Greenland Blocking Patterns. To be Presented at American Geophysical Union Fall Meeting, New Orleans, LA.

Preece, J. R.*, Wachowicz, L. J.*, Mote T. L., Tedesco M. Distinguishing Summer Greenland Blocking Types and their Impact on Greenland Ice Sheet Melt: Long-term trends and association with the North Atlantic Oscillation. Waves to Weather Atmospheric Blocking Virtual Workshop 2021.

Wachowicz, L.J.* and T.L Mote: Arctic Springtime Sea Ice and its Connection to ENSO Variability and Atmospheric Circulation. To be Presented at American Geophysical Union Fall Meeting, December 2021, New Orleans LA.

Wachowicz, L.J.* and T.L. Mote: Springtime Arctic Sea Ice and its Connection to ENSO Variability. To be Presented at American Meteorological Society Annual Meeting, 35th Climate Change and Variability Conference, January 2022, Houston TX.

**B. Awards over the 3-year grant duration:**

AMS student poster award winner: Cartwright, N., G.R. Henderson, B.S. Barrett, 2020: Extreme Blocking in the North Atlantic Arctic in Future Climates. American Meteorological Society Annual meeting, Boston, MA, January 2020.

UGA graduate student L. Wachowicz received and accepted a fellowship through the NCAR Advanced Study Program's Graduate Visitor Program to work with M. M. Holland. The proposed work is to use an Earth systems model to assess the role of low-latitude variability on Arctic sea ice, focusing primarily on the role of moisture transport during Rossby wave breaking. The visit is tentatively scheduled for September - December 2020.